Atmospheric methane since the LGM was driven by wetland sources

Thomas Kleinen[1], Sergey Gromov[2], Benedikt Steil[2], and Victor Brovkin[1]

[1]Max Planck Institute for Meteorology, Bundesstr. 53, 20146 Hamburg, Germany
[2]Max Planck Institute for Chemistry, Hahn-Meitner-Weg 1, 55128 Mainz, Germany

Correspondence: Thomas Kleinen (thomas.kleinen@mpimet.mpg.de)

Abstract. Atmospheric methane (CH_4) has changed considerably in the time between the last glacial maximum (LGM) and the preindustrial period (PI). We investigate these changes in transient experiments with an Earth System Model, focusing on the rapid changes during the deglaciation, especially pronounced in the Bølling Allerød (BA) and Younger Dryas (YD) periods. We consider all relevant natural sources and sinks of methane and examine the drivers of changes in methane emissions as well as

5 in the atmospheric lifetime of methane. We find that the evolution of atmospheric methane is largely driven by emissions from tropical wetlands, while variations in atmospheric lifetime are not negligible but small. Our model reproduces most changes in atmospheric methane very well, with the exception of the mid-Holocene decrease in methane, though the timing of ice sheet meltwater fluxes needs to be adjusted slightly in order to exactly reproduce the variations of the BA and YD.

1 Introduction

10 Between the last glacial maximum (LGM) and the present, the atmospheric concentration of methane (CH_4) changed dramatically. At the LGM, atmospheric CH_4 was at ~380 ppb (Köhler et al., 2017), while it was at 695 ppb at 10 ka BP, thus nearly doubling in concentration during those 11000 yrs. Furthermore, the atmospheric concentration changed very rapidly at four points in time: during the transition from the Oldest Dryas into the Bølling Allerød (BA), during the transition from the BA into the Younger Dryas (YD), and from the YD to the Preboreal (PB) / early Holocene. During each of these transitions

15 atmospheric CH_4 changed by about 150 ppb over a few centuries. Finally, atmospheric methane has more than doubled again between the preindustrial state (1850 CE) and the present (2022 CE). In a previous publication, we investigated the methane emissions during a number of time slices from 20 ka BP to the present (Kleinen et al., 2020). Time slice investigations, however, are very limited in their explanatory power. They rest on the assumption that the system under investigation is in some kind of an equilibrium state, and they give no information at all on how the system might translate between these states. In

20 order to gain insight into highly dynamic changes, transient experiments considering the full dynamics of the system therefore are required. In this publication we present the very first transient deglaciation experiments with a state-of-the-art Earth System Model (ESM) including a complete methane cycle.

Attempts at modelling methane between the LGM and PI go back several decades and mostly fall into one of two categories. Either these were performed with strongly simplified models, typically box models, that only consider very broad spatial

25 aggregations and an extremely reduced process description, for example Chappellaz et al. (1993); Thompson et al. (1993); Fischer et al. (2008). Or they used more detailed process descriptions of at least part of the methane cycle, ranging from the

wetland emissions of methane to a more or less complete description of the methane cycle, for example Valdes et al. (2005); Weber et al. (2010); Singarayer et al. (2011); Zürcher et al. (2013); Hopcroft et al. (2017); Kleinen et al. (2020). These studies were, however, limited to a few time slices, assuming an equilibrium in climate for these time slices and not covering the trajectories connecting these points in time. In this publication we aim to go beyond this state of the art, performing transient experiments with a full ESM specifically adapted to cover the glacial period and the transitions between glacial and interglacial.

The requirements to comprehensively investigate the changes in methane from the LGM to PI are demanding. Ice sheet extent changes by several million km^2, sea level changes by about $130\,m$ (Lambeck et al., 2014), and atmospheric CO_2 increases by roughly 50% from $180\,ppm$ to $280\,ppm$ (Petit et al., 1999). These processes, while affecting methane only indirectly, need to be represented in the ESM in order to reproduce the climatic changes driving the changes in the methane cycle. For the methane cycle itself, the global methane budget (Saunois et al., 2016, 2020) considers emissions of fossil fuels as well as agriculture and waste as anthropogenic emissions. These do not need to be considered here, as our experiments mainly consider the time before anthropogenic emissions become relevant. However, emissions from wetlands and wildfires, as well as several other sources lumped under the 'other natural emissions', namely termites and wild animals, need to be considered, together with the sinks of methane in the atmosphere and soils.

We investigated methane emissions for time slices 5000 years apart from the LGM to the present in Kleinen et al. (2020). We also showed the evolution of atmospheric CH_4 for the next millennium under a number of scenarios in Kleinen et al. (2021). In the present publication we bring these two together and investigate the transient evolution of the methane cycle from the LGM to PI, mainly focusing on the period with the largest changes in climate and methane from 18 ka BP to 10 ka BP, which includes the fast and massive changes during the Bølling-Allerød and Younger Dryas.

2 Modelling the methane cycle in MPI-ESM 1.2

2.1 MPI-ESM 1.2 in transient deglaciation experiments

We use MPI-ESM, the Max Planck Institute for Meteorology Earth System Model (Mauritsen et al., 2019; Mikolajewicz et al., 2018), consisting of the atmospheric general circulation model ECHAM6, the ocean general circulation model MPI-OM, and the land surface model JSBACH in coarse resolution (T31GR30 ≈ 3.75° x 3.75°) to investigate the evolution of atmospheric methane during the deglaciation. The basis for our modelling setup is model version 1.2, the same model version as used in the Coupled Model Intercomparison Project Phase 6 (CMIP6, Eyring et al. (2016)).

MPI-ESM, similar to many other ESMs, considers the land-sea and glacier masks, as well as the river routing, as fixed. For determining the transient evolution of climate, these are updated automatically in our model version, as described in Meccia and Mikolajewicz (2018) and Riddick et al. (2018). Briefly, the model evaluates the changes in ice sheet and sea level after every decade. From these, combined with the RTopo-2 topography (Schaffer et al., 2016), it determines a new land-sea mask, bathymetry and orography, as well as a new river routing setup to be used for the next decade in the model experiment.

2.2 Modelling the methane cycle

Based on the recent Global Carbon Project CH_4 budget (Saunois et al., 2016, 2020), we consider methane emissions from
wetlands, termites, wildfires and herbivores as relevant during the deglaciation, as well as emissions from geological sources.
We assume the latter to be independent of climate and therefore prescribe them, while we aim to model all of the former
interactively. We neglect anthropogenic methane emissions in the experiments described here, as they are highly uncertain but
likely very small for the time period considered in this publication. In terms of methane sinks, the atmospheric sink of methane
is most important, while soils are a secondary sink. We include both of them in our model.

2.2.1 Methane emissions from wetlands, termites and wildfires

The basic methane emission model for emissions from wetlands, termites, and wildfires is described in Kleinen et al. (2020),
we thus cover it only briefly here. We use a TOPMODEL (Beven and Kirkby, 1979) approach to determine inundated areas,
in which we determine the wetland methane emissions based on the model by Riley et al. (2011). Methane emissions from
wildfires and biomass burning are determined from the burned carbon determined in the SPITFIRE fire model (Lasslop et al.,
2014), using emission factors from Kaiser et al. (2012). Termite methane emissions are estimated using the approach from
Kirschke et al. (2013) and Saunois et al. (2016).

In the TOPMODEL approach (Beven and Kirkby, 1979), we combine the soil water content determined in the MPI-ESM
land surface model JSBACH with sub-gridscale topographic information, the Compound Topographic Index (CTI), in order
to determine the variation of the water table in each model grid cell. For our experiments, we use the CTI index product by
Marthews et al. (2015) for the present-day land areas, combined with CTI index values we derived from the the ETOPO1 dataset
(Amante and Eakins, 2009) for those areas that are below sea level at present, using the TOPMODEL R library (Buytaert, 2011).
We then use the variation in water table to determine the inundation fraction, the fraction of each grid cell where the water table
is at or above the surface. In Kleinen et al. (2020) we have evaluated the model for present-day climatic conditions against
remote-sensing data of inundation (Prigent et al., 2012). Total extent and seasonality are similar for the NH extratropics, while
the model slightly overestimates the extent for tropical inundation. We thus assess the agreement between model and data as
reasonable, considering the limitations of both model and remote-sensing data.

In JSBACH the decomposition of soil carbon is described by the YASSO model (Goll et al., 2015), and we assume anaerobic
decomposition in the inundated areas, with decomposition rate constants in YASSO reduced to 35% of the value used for
aerobic decomposition, as proposed by Wania et al. (2010). The anaerobic decomposition of carbon results in production of
both CO_2 and CH_4, with a temperature-dependent partitioning into the two decomposition products as described by Riley et al.
(2011). The transport of O_2, CO_2 and CH_4 is determined in a methane emission model based on Riley et al. (2011), which
explicitly simulates the methane transport via the pathways diffusion, ebullition, and plant aerenchyma. The oxidation of CH_4,
if sufficient oxygen is present, is considered as well, following Michaelis-Menten kinetics. Furthermore the transport model
also determines the soil sink of methane, as CH_4 diffuses into the soil in areas where little methane is produces, i.e. in dry
areas, where it is oxidized subsequently.

Lake methane emissions are not modelled explicitly, but we rather assume that their emissions are implicitly contained in the wetland flux. We make this simplification for pragmatic reasons, as we have not found an appropriate model for lake areas under changing climatic conditions in the literature. We assume, however, that the error introduced by this simplification is relatively minor on the scales the model was designed for (~350+ km spatial resolution, decadal to centennial temporal scale).

95 We base this assumption on two factors: We used surface water extent data to calibrate the wetland model, and this data also contains inland water bodies. Furthermore, we assume that the changes in methane fluxes from inland waters on these scales will be driven by the same factors that drive the changes in wetland emissions, i.e. soil carbon content, temperature, and precipitation. On shorter temporal (monthly to annual) and spatial (10s of kilometers) scales, the errors introduced through this simplification may be significant, though.

100 Methane emissions from wildfires and biomass burning (with the sum subsequently called the 'fire' emissions) are determined from the SPITFIRE fire model (Lasslop et al., 2014), using emission factors from Kaiser et al. (2012). The SPITFIRE fire model determines the spread of fires using the fire ignition probability, a function of lightning frequency and population density (assuming no human population before 12 ka BP and using Klein Goldewijk et al. (2017) afterwards), and flammability (higher under dryer/warmer conditions), as well as the amount of biomass available for burning. The methane emissions are

105 then determined from the burned biomass using emission factors. Termite methane emissions are estimated using the approach by Kirschke et al. (2013) and Saunois et al. (2016), which determines termite mass from gross primary productivity in tropical areas and assumes a constant emission factor to determine the final methane emissions. Geological emissions are prescribed with a spatial distribution from Etiope (2015), but scaled to give a total of $5\,Tg\,CH_4\,yr^{-1}$, based on Hmiel et al. (2020).

In Kleinen et al. (2020) we evaluated the modelled methane emissions for present-day (PD) climate. As flux measure-

110 ments on appropriate scales are not available, we compared aggregate fluxes against global assessments (Saunois et al., 2016). We found that the model simulates wetland methane emissions of $222\,Tg\,CH_4\,yr^{-1}$ (decadal mean over 2000-2009), reduced to $190\,Tg\,CH_4\,yr^{-1}$ for this publication as detailed below, fire emissions of $17.6\,Tg\,CH_4\,yr^{-1}$, termite emissions of $11.7\,Tg\,CH_4\,yr^{-1}$, and a soil uptake of $17.5\,Tg\,CH_4\,yr^{-1}$. These values fall well within the ranges reported by Saunois et al. (2016), who report $153 - 227\,Tg\,CH_4\,yr^{-1}$ for natural wetlands, $15 - 20\,Tg\,CH_4\,yr^{-1}$ for biomass burning, $1 - 5\,Tg\,CH_4\,yr^{-1}$

115 for wildfires, $3 - 15\,Tg\,CH_4\,yr^{-1}$ for termites, and $9 - 47\,Tg\,CH_4\,yr^{-1}$ for the soil uptake. Spatial patterns of PD emissions are also similar to those shown by Saunois et al. (2016). Furthermore, wetland methane emission estimates from atmospheric inversions (Bousquet et al., 2011) show that the majority (62-77%) of the present-day emissions come from regions between 30°S and 30°N, while a much smaller part (20-33%) is emitted north of 30°N. Of the modelled total wetland CH_4 emissions for PD conditions, 70% are from low latitude regions, while 29% are from regions north of 30°N. The latitudinal distribution

120 of modelled PD wetland methane emissions therefore is well within the range obtained from atmospheric inversions.

In order to accommodate the additional methane flux from the consideration of herbivorous mammals in the present publication, we re-calibrated the wetland emission model in comparison to Kleinen et al. (2020), reducing wetland emissions to $190\,Tg\,CH_4\,yr^{-1}$ for the 2000-2009 CE decadal mean, thus keeping total emissions for the present-day roughly constant, despite the additional consideration of herbivore emissions.

2.2.2 Methane emissions from herbivores

At present, methane emissions from herbivores, especially cows, make up a significant part of the methane emissions (Saunois et al., 2020). This fact is, however, the result of human action, as it has to be assumed that the number of ruminants was significantly smaller before humans began herding cows. Previous approaches to estimate the methane emissions from herbivores (Crutzen et al., 1986; Chappellaz et al., 1993; Hristov, 2012; Smith et al., 2016) generally start from the level of individual animals, relating methane emissions to species and body mass. They then rely on estimates of population numbers for specific species to determine total emissions from herbivores. In order to apply such an approach in the context of an Earth System model and past climate states, one would need to somehow relate population densities of certain species via vegetation productivity to climate – which we found impossible to do due to a lack of data, especially for ecosystems untouched by humans, as none of these exist any more. Furthermore, a recent review of methane production by mammal herbivores (Clauss et al., 2020) found that CH_4 yields (CH_4 production per dry matter (DM) intake) do not vary significantly with body mass and between ruminants and non-ruminants, thus negating two of the foundations of the previous approaches to estimating herbivore methane emissions. Instead, they found that absolute CH_4 emissions scaled linearly with DM intake, which allows a simplified treatment of herbivore methane emissions in our model.

As part of the carbon cycle representation, the JSBACH model determines a carbon flux $F_{herbivory}$ from herbivory (Schneck et al., 2013; Reick et al., 2021). Here, $F_{herbivory} = r_{herbivory} \times C_G$ with $r_{herbivory}$ a PFT-dependent constant and C_G the carbon content in the 'green' carbon pool, i.e. the carbon pool representing the living parts of plants (leaves, fine roots, vascular tissues). We further assume that a fraction f_{mammal} of the herbivory flux is consumed by mammals, with $f_{mammal} = 0.016$ in forest and $f_{mammal} = 0.32$ in grasslands. These latter values were chosen ad hoc but seem plausible. Finally, we use a CH_4 yield γ of $\gamma = 14.9\,g(CH_4)\,kg(DM)^{-1}$, obtained as a mean over the values for all species listed in Clauss et al. (2020). The final CH_4 flux from herbivory H_{CH4} thus is:

$$H_{CH4} = f_{mammal} \times \gamma \times F_{herbivory} \tag{1}$$

2.3 Atmospheric methane sink

As described in Kleinen et al. (2021), the spatiotemporal evolution of the methane abundance in the atmospheric model ECHAM6 is simulated using a methane tracer which undergoes transport and chemical removal, while emissions are calculated using the land surface model JSBACH. The atmospheric sink of methane is calculated using a zonally averaged reactivity field obtained from the comprehensive ECHAM/MESSy Atmospheric Chemistry Model (EMAC) (Joeckel et al., 2010). Following Gromov et al. (2018) and Kleinen et al. (2021), the following updated parameterisation is used to account for variations in atmospheric oxidative capacity and therefore tropospheric CH_4 reactivity r_{CH_4}:

$$r_{CH_4} = \alpha \times (LN + k_N RN)^p \times (M + k_C RC + k_A A)^q \,[yr^{-1}] \tag{2}$$

155   with LN being the global lightning nitrogen oxides (NO$_X$) emission, simulated interactively according to Price and Rind (1992, 1993), M the CH$_4$ atmospheric burden, RN and RC the terrestrial (surface) emissions of reactive nitrogen (NO$_X$) and carbon compounds given in TgN and TgC per yr for the emission fluxes, respectively, and A the mean tropospheric reactive aerosol surface area (about $100\,Mm^2$ in both present-day and past climates). Fit parameters ($\alpha = 7.45\,TgN^{-p}TgC^{-q}yr^{-1}$, $p = 0.36$, $q = -0.60$, $k_N = 0.59$, $k_C = 4.25$, $k_A = 4.21\,TgC/Mm^2$) are obtained from an ensemble of EMAC simulations

160   covering a broad range of RN, RC, LN and M values in the LGM (21 ka BP), Mid-Holocene (6 ka BP), PI and present-day conditions. The fitted r_{CH_4} value is accurate to 7% at 95% CI. In the MPI-ESM experiments, the natural emission components of RN and RC are obtained from the MEGAN model (Guenther et al., 2012) for the biogenic sources and from the SPITFIRE model (Lasslop et al., 2014), with emission factors from Kaiser et al. (2012), for fire emissions. We use the terrestrial NO$_X$ emissions for the RN term, and for the RC term we use biogenic CO and isoprene (C$_5$H$_8$) fluxes, scaled by a factor of 1.4 to

165   account for secondary biogenic co-emitted compounds, as proxies for the total RC emitted. These scaling factors were derived from the simulated present-day total RC emissions. In experiments covering the historical and future periods, anthropogenic emissions of RC and RN would be considered as well (see Kleinen et al. (2021)), but are neglected for the experiments described in this publication.

2.4   Model forcing and experiments

170   We forced the model with prescribed orbital parameters from Berger (1978) and greenhouses gases from Köhler et al. (2017). Orbital parameters and greenhouse gas concentrations are supplied to the model as decadal means and are updated every 10 model years. Atmospheric aerosols were prescribed to constant 1850 conditions (Kinne et al., 2013), and we considered no anthropogenic land use. Ice sheet extent was prescribed from the GLAC-1D ice sheet reconstruction (Tarasov et al., 2012; Briggs et al., 2014; Ivanovic et al., 2016). Ice sheet extent, as well as bathymetry and topography (Meccia and Mikolajewicz,

175   2018) and river routing (Riddick et al., 2018) were continuously updated every 10 model years.

    Methane emissions from geological sources were prescribed using a spatial distribution from Etiope (2015), but scaled down to give total geological methane emissions of $5\,TgCH_4yr^{-1}$, as Petrenko et al. (2017) and Hmiel et al. (2020) show from ice-core data that geological emissions larger than this value are not possible for either the Younger Dryas or the preindustrial period.

180   We initialised the model from a spinup experiment at constant 26 ka BP boundary conditions, running for several millennia. From this model state, we performed a transient model experiment until preindustrial times, with continuously updated ice sheet extent, bathymetry, topography, and river routing, similar to the experiments described by Kapsch et al. (2022). In this experiment, called *base* in the following, the prescribed ice sheet forcing from the GLAC-1D reconstruction leads to a collapse of the Atlantic MOC early in the Bølling-Allerød (Kapsch et al., 2022), due to excess meltwater entering the North Atlantic,

185   and the Younger Dryas does not occur in this experiment. Thus we performed a second experiment, called *MWM* (meltwater manipulation), where we manipulate the meltwater fluxes from the Laurentide ice sheet: Starting in 15.2 ka BP, we prevent meltwater from the Laurentide ice sheet from reaching the ocean, instead storing it. We then release this accumulated meltwater

over a period of 1200 years, starting in 12800 BP, adding it to the Mackenzie River watershed, thus mimicking the storage of glacial meltwater in proglacial lakes like Lake Agassiz and its subsequent release (Murton et al., 2010).

3 Results

3.1 Transient climate and land carbon changes

At the last glacial maximum, around 20 ka BP, the global mean temperature is $282K$ in our model, $4.7K$ lower than at PI (Fig. 1a). As the ice sheets melt and CO_2 increases, the temperature begins to rise significantly after 18 ka BP, with the rate of temperature increase declining after 9 ka BP. Dallmeyer et al. (2022) evaluated model temperatures in the experiment against reconstructions and found a reasonably close match. The AMOC (Fig. 1b) is relatively stable at about $20\,Sv$ between the LGM and 14.8 ka BP. Here the *base* and *MWM* experiments diverge: in the *base* experiment meltwater pulse (MWP) 1a leads to a strong freshening of the North Atlantic and a near complete AMOC shutdown (remaining overturning of $1\,Sv$) at 14.38 ka BP, which in turn leads to a drop in global mean temperature by nearly $1K$. Temperature and AMOC recover quickly, however. The AMOC continues to be highly variable until 9 ka BP, with a further near collapse from MWP 1b at 11.4 ka BP. Global mean temperature, however, is affected significantly less by the AMOC reduction at MWP 1b than at MWP 1a. After 9 ka BP, the AMOC is relatively stable, though at a slightly smaller overturning of $18.7\,Sv$ (at PI). Similar to global mean temperature, the total land carbon stock (Fig. 1c) stays nearly constant at $970\,PgC$, $718\,PgC$ less than at PI, from LGM to 18 ka BP. Subsequently total land C increases until 10.95 ka BP. Afterwards only minor changes in total land carbon stock occur until the PI state with a total land C stock of $1688\,PgC$. The AMOC collapse at 14.38 ka BP caused by MWP 1a leads to a short decrease in C stock by about 6.8%, but the total duration of this excursion is about 800 years, and carbon continues to rise after it.

In the *MWM* experiment, the initial collapse of the AMOC at 14.38 ka BP is prevented by the manipulation of the meltwater fluxes, and temperature and carbon continue to rise during this period. As we release the accumulated Laurentide ice sheet meltwater at 12.8 ka BP, the AMOC collapses, with the consequence of a drop in global mean temperature by $1.25K$ and a decrease in terrestrial C stock by $100\,PgC$ or 6.9%. After we end the meltwater manipulation in 11.6 ka BP, temperature, AMOC and land carbon stocks recover quickly.

3.2 Transient changes in methane

In comparison to a stack of ice-core derived CH_4 concentration in Antarctica (Köhler et al., 2017), the atmospheric concentration of methane in our experiments is quite reasonable overall (Fig. 2a), although there are significant discrepancies during some periods. In the ice-core, methane is nearly constant at ~$370\,ppb$ from LGM to 18 ka BP, when it starts increasing slowly. At 14.6 ka BP, the transition into the Bølling-Allerød warm period, CH_4 increases abruptly by ~$150\,ppb$, decreasing again at 12.8 ka BP, the transition into the Younger Dryas. At the end of the YD, at about 11.5 ka BP, CH_4 again increases abruptly and stays roughly constant at ~$690\,ppb$ for the next 2000 yrs. Finally, ice core CH_4 slowly decreases by ~$120\,ppb$ during the early Holocene between 9 ka BP and 4.5 ka BP, recovering after the mid Holocene to ~$690\,ppb$ at PI.
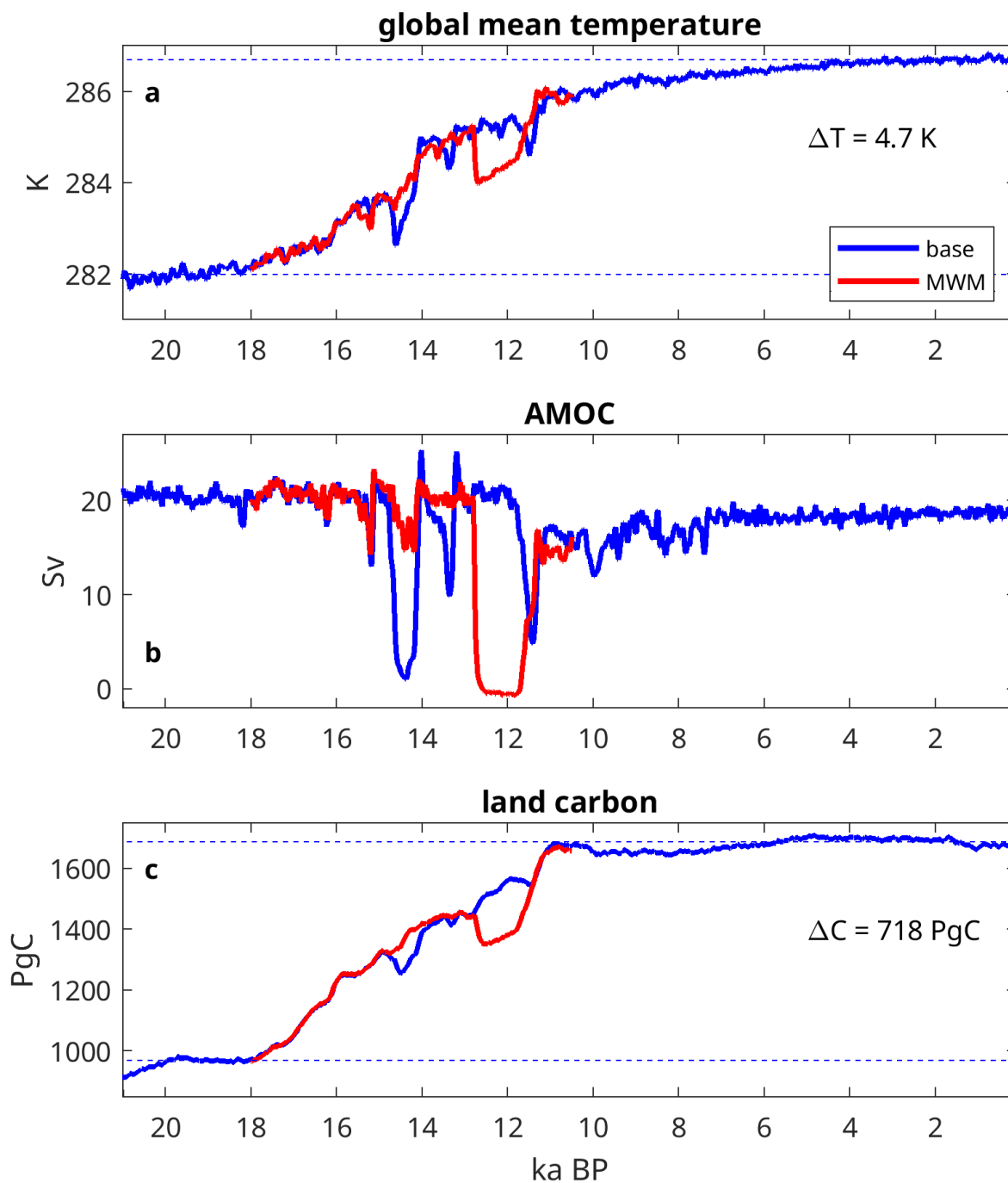
Figure 1. Overview over climatic and land carbon changes from LGM to PI: Global mean temperature (a), North Atlantic meridional overturning circulation (b), total land carbon storage (c). *Base* experiment in blue, *MWM* experiment in red.
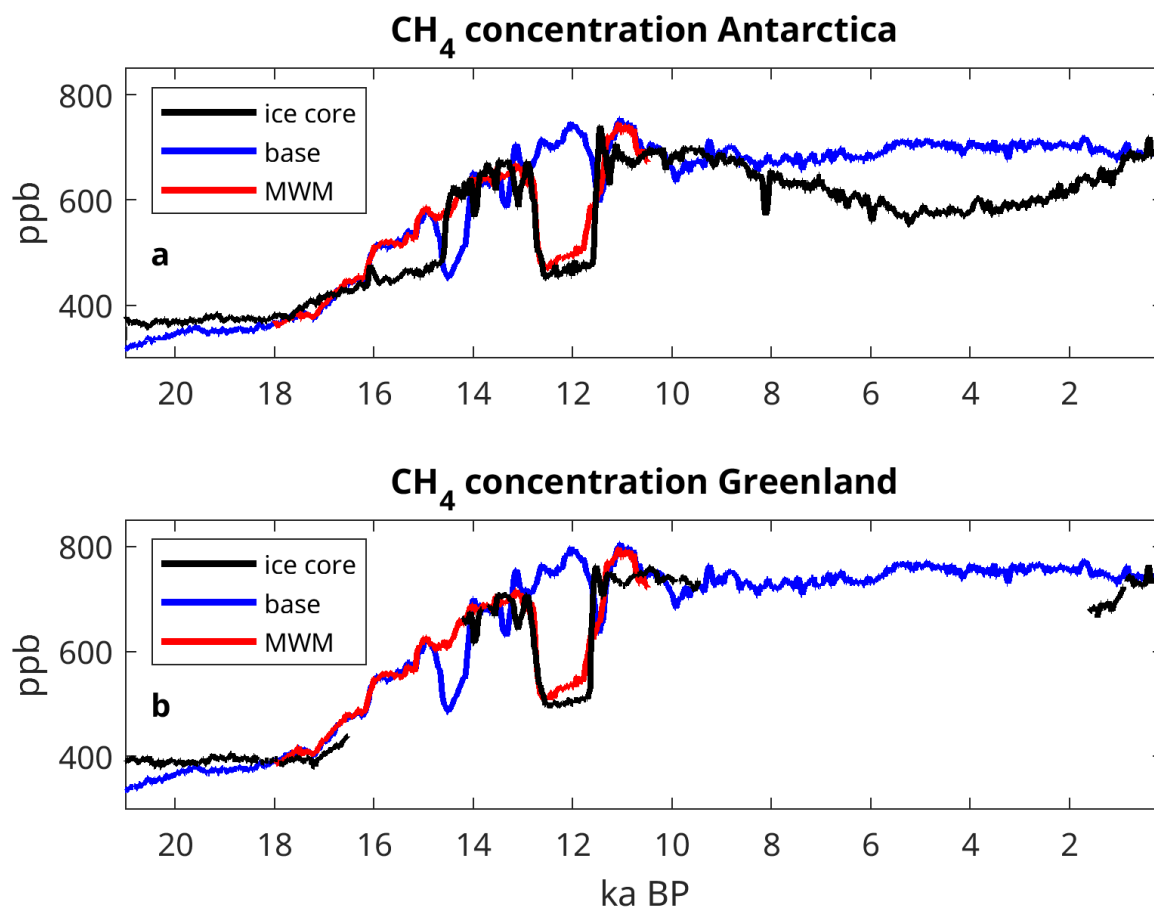
Figure 2. Atmospheric concentration of CH$_4$ over Antarctica (a) and Greenland (b) in MPI-ESM *base* and *MWM* experiments, as well as ice core data. Antarctic ice core data from Köhler et al. (2017) and Greenland ice core data from Chappellaz et al. (2013) and Rhodes et al. (2013).

Timeslice	LGM	early BA	late BA	early YD	early Holocene
	20 ka	14.2 ka	12.9 ka	12.5 ka	10.6 ka
Antarctica:					
base	350	540	660	710	700
MWM	n/a	620	630	480	680
ice core	370	620	660	460	690
Greenland:					
base	370	580	710	760	750
MWM	n/a	663	680	510	730
ice core	390	660	700	500	750

Table 1. Simulated and reconstructed CH_4 concentrations [ppb] at the ice core sites for selected timeslices.

Modelled atmospheric CH_4 over Antarctica is only slightly lower than reconstructed at 20 ka BP (370 ppb ice core, 350 ppb

220 model, Table 1), though the discrepancy is larger at 21 ka BP. Similar to reconstructions, the atmospheric CH_4 starts rising significantly at 18 ka BP, but the increase at the beginning of the Bølling-Allerød and the drop in methane during the transition into the Younger Dryas are dissimilar, at least in the *base* experiment: In terms of atmospheric CH_4 the Bølling-Allerød seems to start earlier, at 16 ka BP instead of 14.6 ka BP. At 14.38 ka BP, near the beginning of the B-A in reconstructions, the *base* experiment displays a significant drop in atmospheric methane, caused by the AMOC shutdown after MWP 1a. For the

225 transition into the Younger Dryas at 12.8 ka BP, on the other hand, the *base* experiment continues at high levels of atmospheric methane and does not show the decrease in methane displayed by the ice core data as the model shows no climatic transition at this time.

The *MWM* experiment differs from the *base* experiment at the beginning of the B-A, as the atmospheric concentration of methane does not change at the beginning of the Bølling-Allerød. Instead, it is very similar to the ice core data. Furthermore,

230 the atmospheric concentration of methane very rapidly decreases by 25% at the beginning of the Younger Dryas at 12.8 ka BP, similar to ice core data (-29%). At the end of the Younger Dryas, recovery of atmospheric methane occurs slightly earlier than in the ice core data, but not as quickly. The Younger Dryas in our *MWM* experiment, therefore, is quite similar to the ice core data. For the Holocene atmospheric methane, however, there is a significant divergence between model results and ice-core data: While ice-core CH_4 slowly decreases towards the mid-Holocene and increases again during the late Holocene, the model

235 results show constant atmospheric CH_4 throughout the Holocene.

A comparison to Greenland ice cores is much more intricate, as recent investigations show excess CH_4 in some Greenland ice core records (Lee et al., 2020). This issue has not yet been resolved fully, and we thus do not show a full ice core CH_4 timeseries from Greenland. Instead we focus on data derived from the NEEM ice core (Chappellaz et al., 2013; Rhodes et al., 2013), which has been obtained using a continuous-flow measurement technique and is thus presumably less susceptible to the

240 generation of excess CH_4. For those times when data is available (earlier than 17.5 ka BP, 14-10 ka BP, after 2 ka BP), the comparison for Greenland (Fig. 2b) is similarly good as the comparison for Antarctica . Thus Greenland CH_4 is very similar

for 20 ka BP to 18 ka BP, and the evolution of methane during the Bølling-Allerød - Younger Dryas transition is also very similar in model and ice core data, if one considers the *MWM* experiment (Table 1). Our model thus captures the gradient in methane between Greenland and Antarctica adequately for key periods of the deglaciation.

245   The terrestrial methane fluxes (Fig. 3) largely determine the atmospheric methane concentration. The net CH_4 flux (Fig. 3a) increases from $90\,Tg\,CH_4\,yr^{-1}$ at 20 ka BP to $165\,Tg\,CH_4\,yr^{-1}$ at PI, with emissions staying very similar between 20 and 18 ka BP, then increasing more strongly between 18 and 11 ka BP, while staying nearly constant between 10 ka BP and PI. In the *base* experiment, emissions decrease strongly as a response to the AMOC collapse after MWP 1a, with emissions recovering quickly as the AMOC resumes, a pattern continued after MWP 1b. In the *MWM* experiment, however, we see
250   a reduction in net emissions by $32\,Tg\,CH_4\,yr^{-1}$ in response to the AMOC collapse induced by the meltwater manipulation, followed by a quick recovery as the manipulation ceases. Wetland fluxes (Fig. 3b) are the most important component of the net CH_4 flux, thus their temporal change is rather similar to the net flux, though at a slightly smaller overall magnitude, with wetland emissions of $79\,Tg\,CH_4\,yr^{-1}$ at 20 ka BP and $142\,Tg\,CH_4\,yr^{-1}$ at PI, while the emission reduction from the AMOC collapse in the *MWM* experiment is $32\,Tg\,CH_4\,yr^{-1}$. The non-wetland methane fluxes (Fig. 3c) are of significantly
255   smaller magnitude than the wetland fluxes, with emissions at 20 ka BP of $7.4\,Tg\,CH_4\,yr^{-1}$ for herbivores, $2.8\,Tg\,CH_4\,yr^{-1}$ for termites, $3.2\,Tg\,CH_4\,yr^{-1}$ for fire emissions, and $-2.2\,Tg\,CH_4\,yr^{-1}$ for the methane uptake in upland soils. Towards the PI state, these fluxes increase to $14.5\,Tg\,CH_4\,yr^{-1}$, $6.3\,Tg\,CH_4\,yr^{-1}$, $10.9\,Tg\,CH_4\,yr^{-1}$ and $-6.3\,Tg\,CH_4\,yr^{-1}$ for herbivores, termites, fires and uptake, respectively. Here, the differences between the *base* and *MWM* experiments are small, we thus omit the *MWM* experiment from Fig. 3c. The dynamics of the uptake flux appear different from the other fluxes at first glance, with pronounced
260   differences for Bølling-Allerød and Younger Dryas at the same times as they appear in proxy records. This is due to the fact that the most important driver for the terrestrial methane uptake is the atmospheric concentration of methane (Kleinen et al., 2020), which we prescribed from ice core data for the uptake flux.

       We model the atmospheric sink of methane as a function of terrestrial emissions of reactive carbon (RC), as well as NO_X emissions from the soil/vegetation and lightning (Eq. 2). The temporal changes in RC emissions during the deglaciation
265   (Fig. 4a) are very similar to the changes in CH_4 emissions: At 20 ka BP, RC emissions are $270\,Tg\,C\,yr^{-1}$, and at 18 ka BP these start increasing noticeably, reaching a maximum of $500\,Tg\,C\,yr^{-1}$ at 11 ka BP. They are nearly constant, with a very small increasing trend during the Holocene, with values increasing from $477\,Tg\,C\,yr^{-1}$ at 8 ka BP to $490\,Tg\,C\,yr^{-1}$ at PI. The *base* experiment also contains interruptions of the increasing trend after MWP 1a and 1b, which do not occur in the *MWM* experiment. The latter instead displays a significant decrease in RC emissions during the Younger Dryas. Surface NO_X emissions
270   (Fig. 4b) increase much more gradually than RC emissions, though at a higher relative rate, with total fluxes of $2.2\,Tg\,N\,yr^{-1}$ and $5.8\,Tg\,N\,yr^{-1}$ at 20 ka BP and PI, respectively. They also are much less affected by AMOC fluctuations, thus not having as strong a response to MWPs 1a and 1b in the *base* experiment, or the meltwater-induced AMOC collapse in the *MWM* experiment. As a result, the two experiments do not differ significantly in terms of terrestrial NO_X emissions. This is different for the lightning NO_X emissions (LNO_X), which have a minimum of $1.6\,Tg\,N\,yr^{-1}$ at LGM and increase to $2.4\,Tg\,N\,yr^{-1}$ at 9 ka BP,
275   decreasing thereafter to $2.2\,Tg\,N\,yr^{-1}$ at PI. Decreases after MWPs 1a and 1b are clearly visible in the *base* experiment; in the *MWM* experiment, LNO_X reduces from $2.2\,Tg\,N\,yr^{-1}$ during the BA to $1.9\,Tg\,N\,yr^{-1}$ during the YD.

net CH$_4$ emission

a

TgCH$_4$ yr^{-1}

base
MWM

wetland CH$_4$ emissions

b

TgCH$_4$ yr^{-1}

non-wetland CH$_4$ emissions

c

TgCH$_4$ yr^{-1}

herbivores
fires
termites
uptake

ka BP
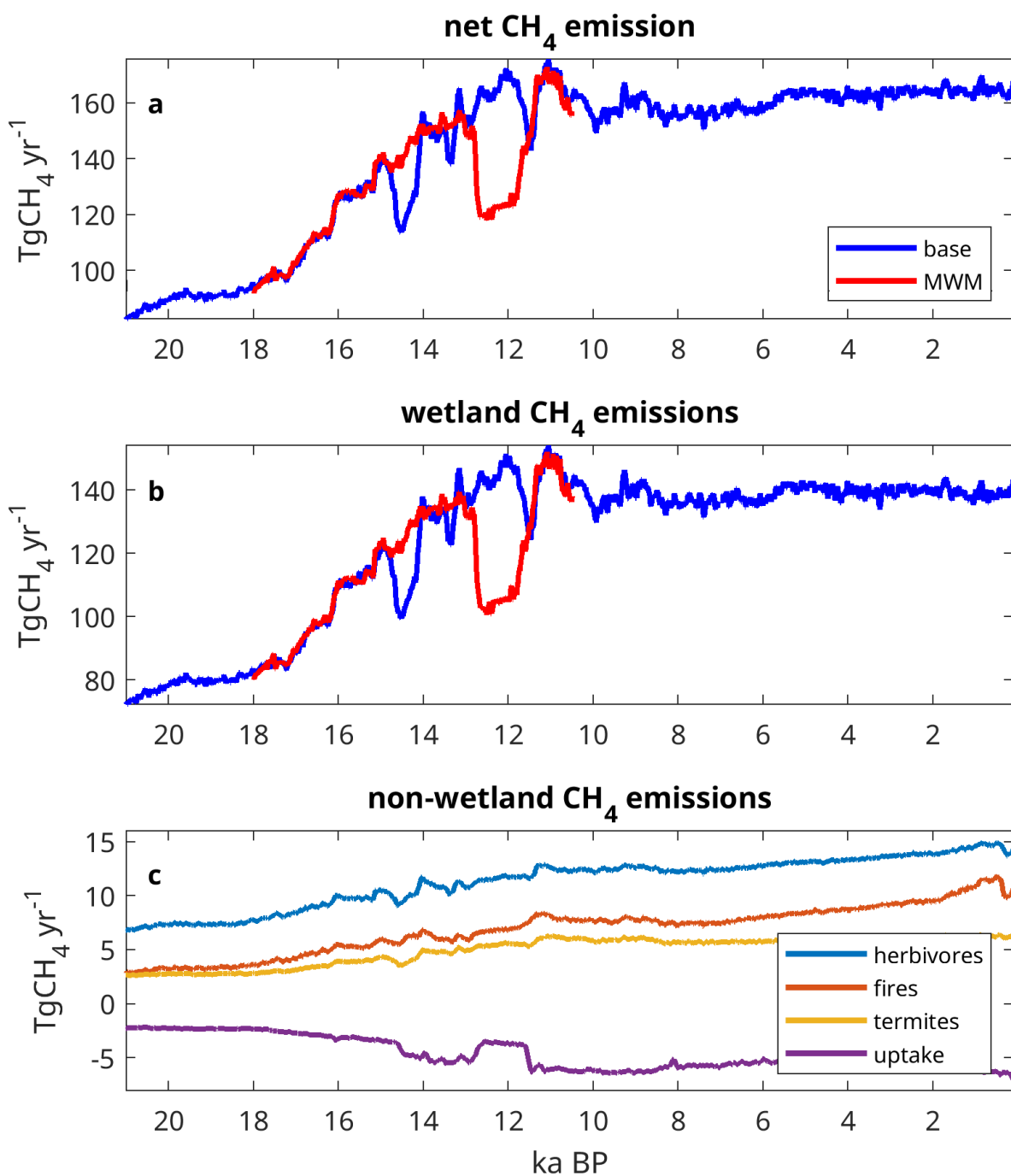
Figure 3. Terrestrial methane in MPI-ESM *base* and *MWM* experiments: (a) net flux, (b) wetland emission flux, (c) non-wetland methane emissions from herbivores, fires, termites and terrestrial methane uptake.

Climate
of the Past
Discussions

EGU
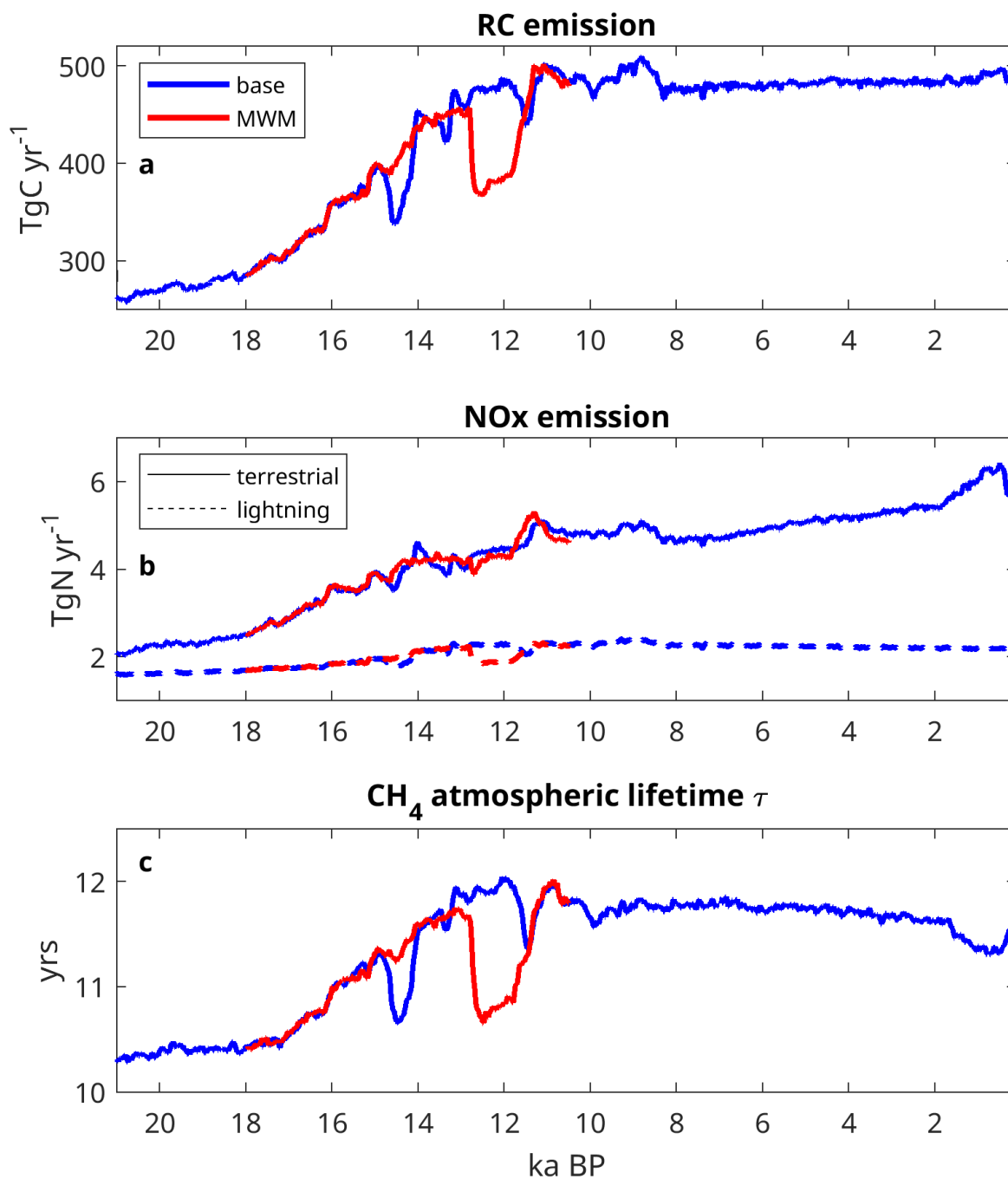
Figure 4. Atmospheric sink of CH$_4$: Emissions of reactive carbon (RC) (a), NO$_X$ from soils and lightning (b) and resulting atmospheric lifetime τ of CH$_4$ (c). τ increases with increasing RC and decreases with increasing NO$_X$.

In both experiments, the simulated atmospheric lifetime of CH_4 (Fig. 4c) varies considerably, from $10.4\,yrs$ at 20 ka BP to a maximum of $12\,yrs$ at 12-11 ka BP, slowly decreasing throughout most of the Holocene, from $11.8\,yrs$ at 8 ka BP to $11.6\,yrs$ at 2 ka BP, and a departure to $11.3\,yrs$ at 1 ka BP, before reaching $11.6\,yrs$ at PI. Prior to about 8 ka BP, the variations are
280   dominated by pronounced changes in RC emissions and CH_4 burden. Note that larger RC emissions and CH_4 burden increase methane lifetime, whereas larger NO_X emissions have the opposite effect. The general tendency towards higher NO_X emissions is damping the RC-driven increase in methane lifetime. Consequently, the reduction in RC emissions driven by the meltwater events results in a stronger decrease in methane lifetime, since the total NO_X emissions are much less effected by these events. LNO_X is reduced, but soil NO_X is unaffected and even slightly increasing.

285   ## 3.3   The Bølling-Allerød and Younger Dryas

The model experiments we performed do not display the signature in methane concentration expected for the onset of the Bølling-Allerød, an abrupt increase in atmospheric methane between 14.6 ka BP and 14.5 ka BP. Instead, we see an abrupt increase in atmospheric methane at 16.2 ka BP, 1.6 ka earlier than expected from paleoclimate reconstructions. What is missing in the model experiments, too, is the AMOC signature that would be associated with Heinrich event 1 (H1), a near collapse
290   as recorded in Bermuda rise sediments (McManus et al., 2004; Stanford et al., 2011). Due to the absence of the H1, the Bølling-Allerød thus occurs earlier in our model, and is initially of smaller magnitude.

Comparing net CH_4 emissions between the late BA at 13.2 ka BP in the *MWM* experiment and 20 ka BP (Fig. 5), increases in emissions are apparent south of the NH ice sheets, as well as in Siberia. The most prominent increase in emissions, however, occurs in the NH tropics, with increases in Africa and Asia especially prominent. Especially northern Africa is substantially
295   wetter and greener than either at LGM or at present, with the substantial CH_4 emissions from the Sahel region very striking. The increase in precipitation here leads to an expansion of wetlands and vegetation, and while the wetland expansion increases the methane emitting area, the expansion of vegetation enhances soil carbon content, thus increasing the substrate available for methane generation.

As the AMOC collapses due to the induced meltwater release at 12.8 ka BP, the region around the North Atlantic Ocean
300   becomes substantially colder, with temperature decreases exceeding $-5K$ in large parts of the Northern and Eastern Atlantic Ocean basin north of the equator. Precipitation in the NH tropics also decreases significantly, with decreases of more than $-1000mm\,yr^{-1}$ in the tropical Atlantic and precipitation decreases of more than $-400mm\,yr^{-1}$ in the Sahel region, as well as over India and Indonesia. As a result, methane emissions decrease substantially between the BA at 13.2 ka BP and the YD at 12.5 ka BP (Fig. 6). Most significant are methane emission reductions all over the tropics, largely due to reduced precipitation
305   leading to less methane production, but also in Europe, where conditions are substantially colder and dryer during the YD than during the BA.

3.4   The role of exposed shelf areas

Due to the lower sea level in glacial climate, significant areas of the present-day continental shelf were exposed. In our model, $14.2 \times 10^6 km^2$ of non-glaciated continental shelf that lie below sea level at present were exposed at 20 ka BP. Slightly more
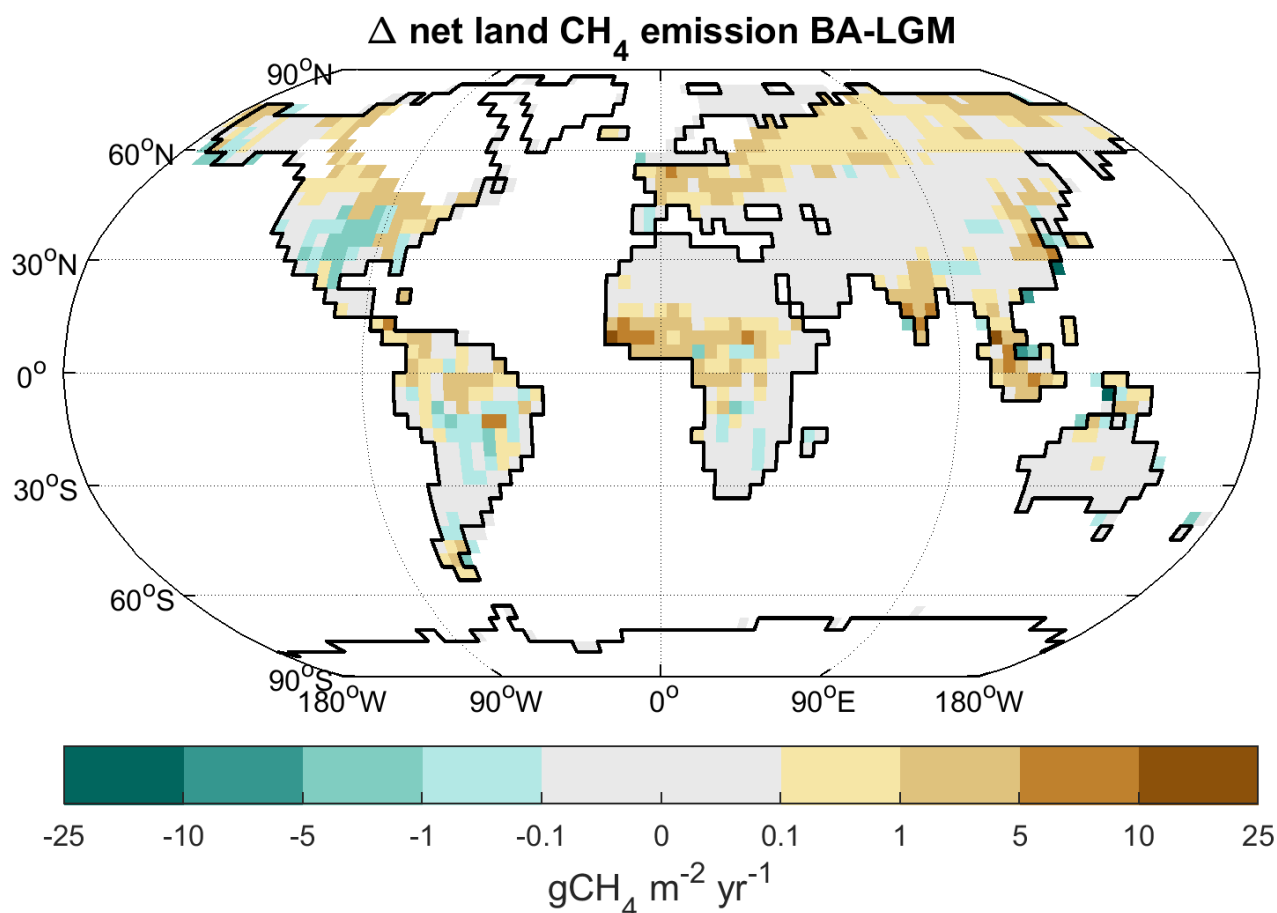
Figure 5. Change in net land CH$_4$ emissions between LGM (20 ka BP) and BA (13.2 ka BP) in *MWM* experiment. Shaded areas indicate LGM land points, continental outline is from 13.2 ka BP.

310 than half this area ($7.8 \times 10^6 km^2$) was located in tropical latitudes, predominantly in South-East Asia and Australia. In the NH extratropics, some $5 \times 10^6 km^2$ were exposed, largely in the Laptev Sea and Bering Strait. These areas changed relatively little until 15 ka BP, but started decreasing rapidly afterwards. By 7.8 ka BP most of these areas were flooded, and at 4.3 ka BP the rising sea level covered the remainder. Our model shows the exposed shelf areas to be a significant source of methane due to significant vegetation growth and wetland formation. With emissions of $31\,Tg CH_4\,yr^{-1}$, the global shelf areas emitted a

315 significant fraction of the net methane flux at 20 ka BP (Fig. 7a). Due to global warming, the shelf emissions increased further to $40\,Tg CH_4\,yr^{-1}$ at 15 ka BP, but declining subsequently as sea level rise started to submerge these areas. The bulk of this flux – $20\,Tg CH_4\,yr^{-1}$ at 20 ka BP – is emitted from the extensive shelf areas in South-East Asia (Sunda shelf) and north-western Australia (Sahul shelf), combined in Fig. 7b as South East Asia. Here, emissions increased slightly between 20 ka BP and 14

Δ net land CH$_4$ emission YD-BA
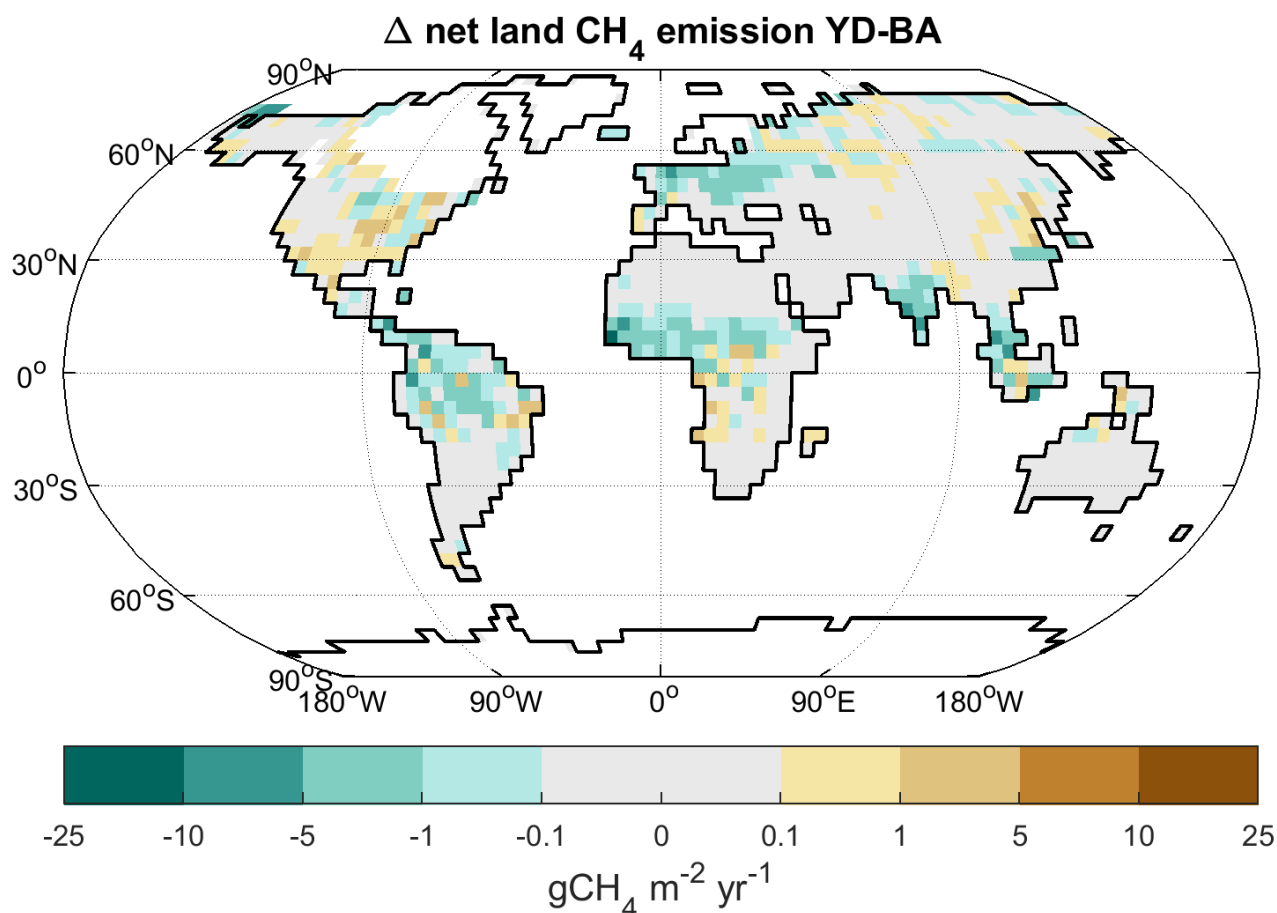
Figure 6. Change in net land CH$_4$ emissions between BA (13.2 ka BP) and YD (12.5 ka BP) in *MWM* experiment. Shaded areas indicate BA land points, continental outline is from 12.5 ka BP.

ka BP, subsequently dropping to near zero by 10 ka BP. While the AMOC collapse in the meltwater manipulation experiment
320 does affect the region, decreasing emissions slightly, the effect is less pronounced here than in other regions. In non-tropical
regions, the largest exposed shelf area in the Laptev Sea and Bering Strait had emissions of some $3.2\,TgCH_4\,yr^{-1}$ at 20 ka BP,
which rose to $6.9\,TgCH_4\,yr^{-1}$ at 14 ka BP, falling subsequently to zero at 8 ka BP when the remaining shelf area was flooded.

There were further regions with some shelf methane emissions, but the aforementioned areas cover the most important
source regions at 15 ka BP (Fig. 8). However, the highest net emissions originate in a grid point in the East China Sea, just east
325 of present-day Shanghai. The bathymetric data used to determine wetland area on the shelves indicates a very flat area at this
location, which results in a grid-cell mean inundation of nearly 25% at 15 ka BP. Whether this high value accurately reflects
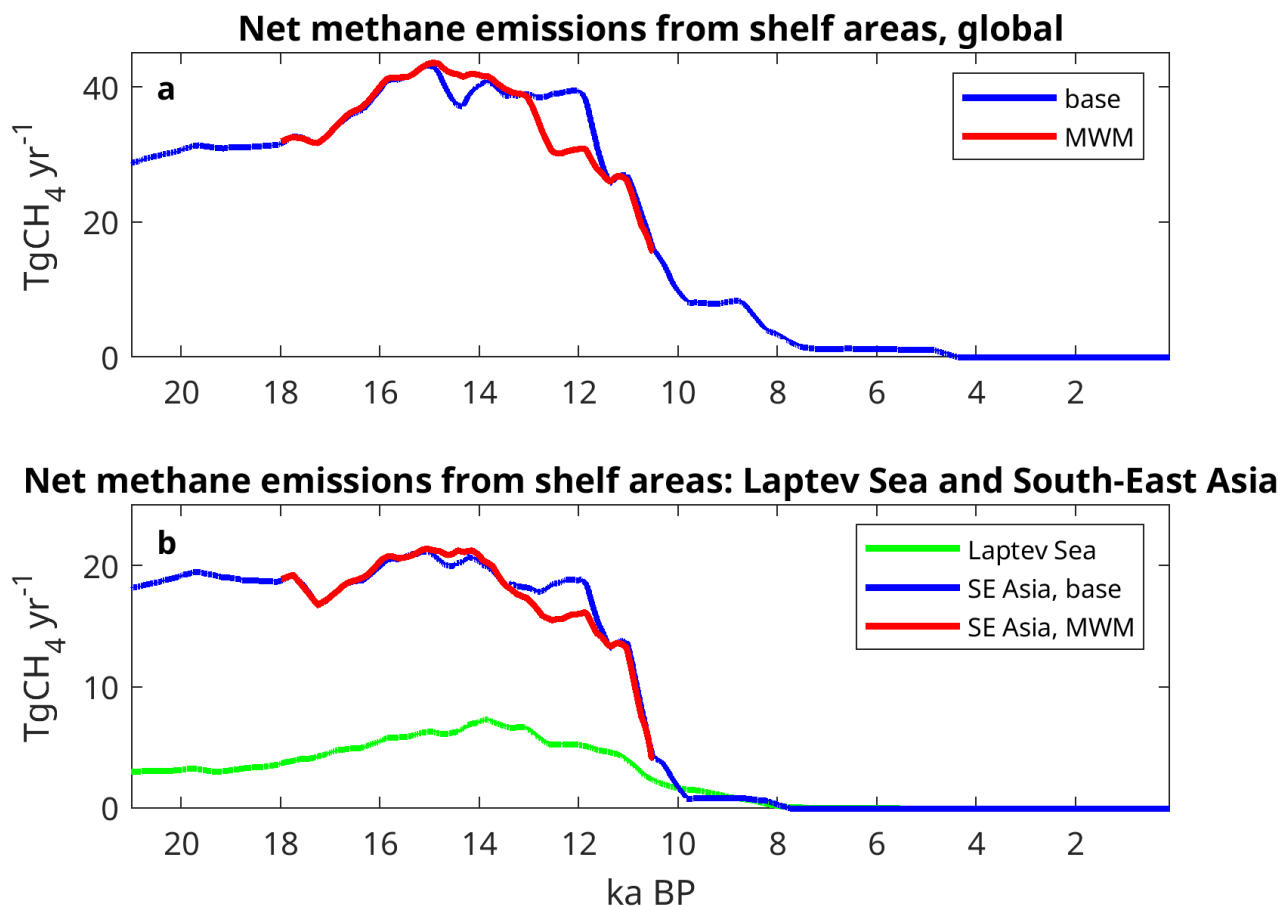
Figure 7. Net methane emissions from shelf areas flooded in PI climate. Global emissions (a) and emissions from Laptev Sea and South-East Asia (b).

conditions at the time when the shelf was exposed, or whether it is due to subsequent changes in bathymetry caused by the Yangtze river sediment load is an open question we are not qualified to answer.

3.5 Orbital influence on Holocene methane emissions

330 During the early Holocene, at 9 ka BP, the total methane emissions were very similar to the PI state. However, the spatial distribution differed significantly (Fig. 9). Due to the recent deglaciation of North America, with some parts of the Laurentide ice sheet still remaining, CH_4 emissions from North America were strongly reduced, while emissions from northern Siberia were enhanced in comparison to PI, due to enhanced vegetation growth (and thus soil carbon) from increased solar radiation during the boreal summer season. Furthermore, emissions from South America were reduced. The most striking difference to
335 the PI state, though, were the changes in NH tropical Africa. At present, northern Africa is not an important source of methane.

shelf net CH$_4$ emission 15 ka BP
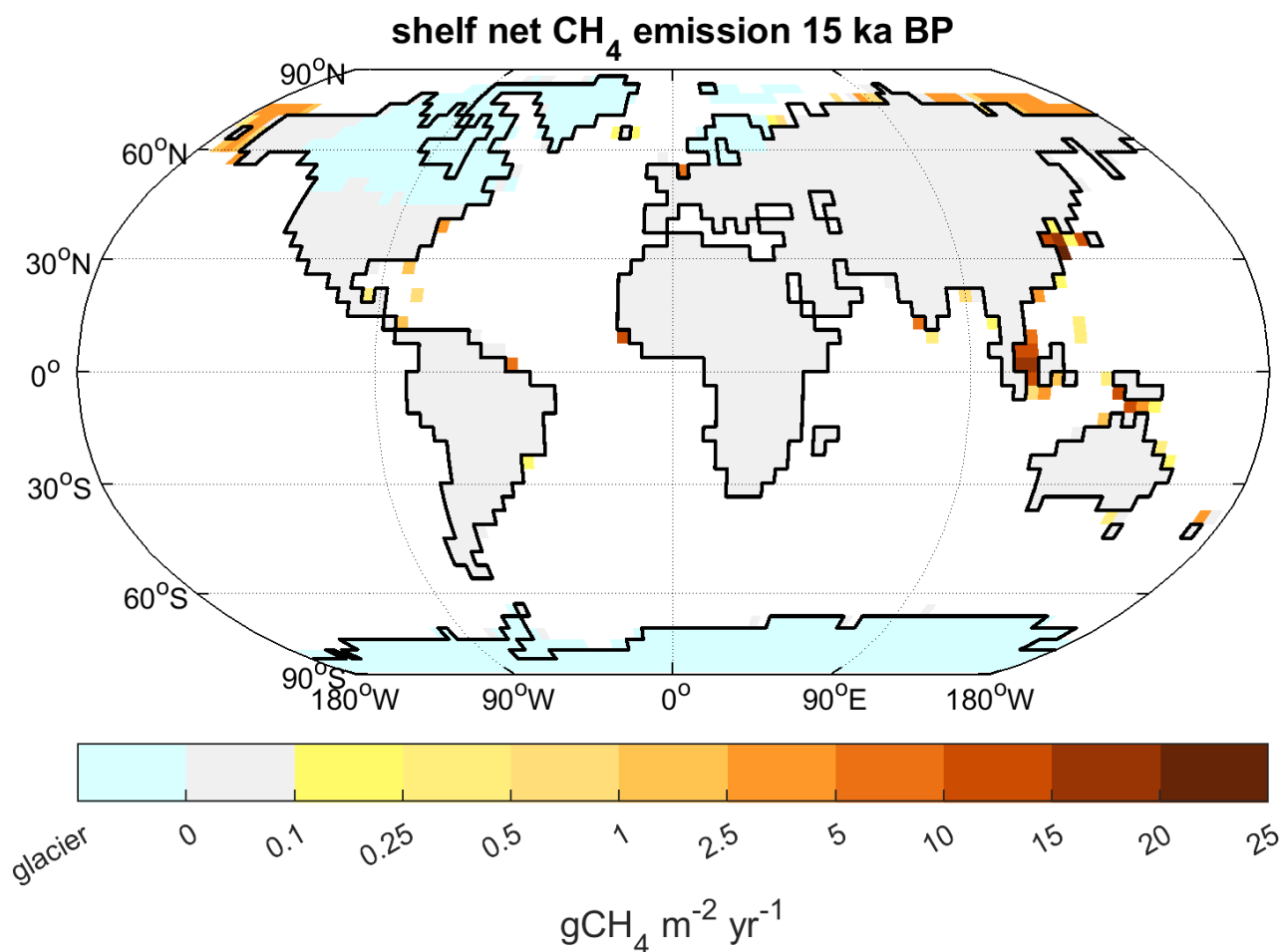
Figure 8. Net shelf CH$_4$ emissions at 15 ka BP, the emission maximum. Shaded areas indicate land points at 15 ka BP, continental outline is from the PI state.

Large parts of the continent are rather dry, thus not producing significant amounts of methane. During the early Holocene, however, the North African monsoon was considerably stronger, leading to significantly enhanced precipitation across the Sahel region, reaching into the southern Sahara (Fig. 10) (Dallmeyer et al., 2020, 2021). As a result, vegetation and wetlands in the Sahel expanded and methane emissions were substantially stronger than at PI.

340   Looking at the timeseries of the regional distribution of methane fluxes since the LGM in our experiments, the SH tropics had the largest net emissions at LGM, with NH tropics and extratropics each having slightly lower emissions. As emissions increased during the deglaciation, their share in the NH tropics and extratropic increased faster than that from the SH tropics (Fig. 11a). Emissions in the NH extratropics increased markedly between 18 ka BP and 11 ka BP, rising from $33\,Tg\,CH_4\,yr^{-1}$ to $60\,Tg\,CH_4\,yr^{-1}$ 7000 years later, with little change afterwards. Emissions in the NH tropics, on the other hand, were strongly
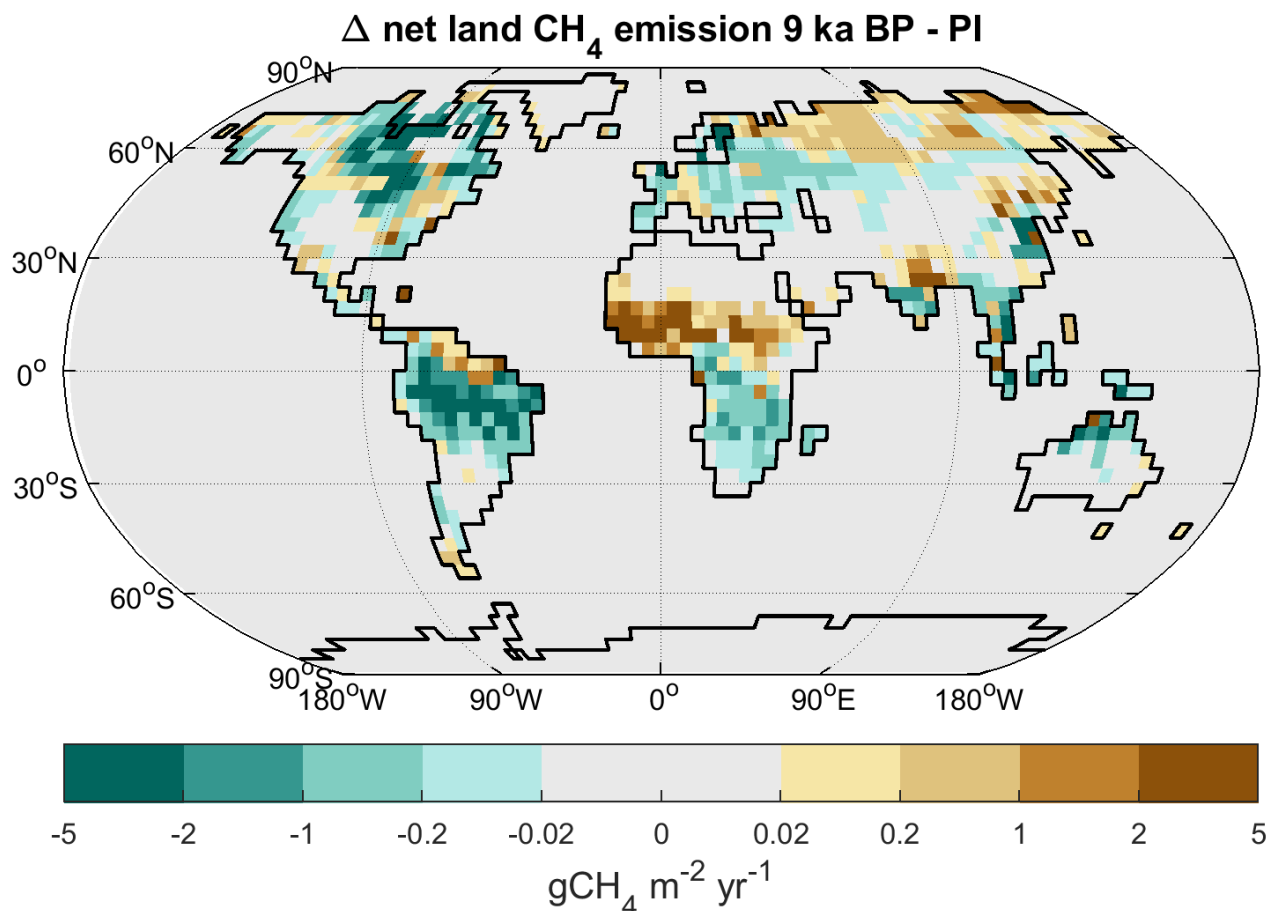
Figure 9. Net CH$_4$ emission change 9 ka BP - PI, continental outline is from 9 ka BP.

345   affected by the AMOC perturbation events, after MWP 1a in the *base* experiment and at 12.8 ka BP in the *MWM* exper-
iment. Here, emissions also started to increase from $30 \, TgCH_4 \, yr^{-1}$ at 18 ka BP, and they continued to rise until reaching
$62 \, TgCH_4 \, yr^{-1}$ at 9 ka BP. In the *base* experiment, this increase was interrupted after MWP 1a, here CH$_4$ emissions dropped
from 46 to $27 \, TgCH_4 \, yr^{-1}$ during the period from 15 to 14.4 ka BP. In the *MWM* experiment, on the other hand, emissions
in the NH tropics strongly reacted to the imposed Younger Dryas event, with emissions dropping from 55 to $31 \, TgCH_4 \, yr^{-1}$
350   between 12.8 and 12.5 ka BP. Investigating the changes in the NH tropics by continent (Fig. 11b), it is clear that the bulk of
the long-term changes in methane fluxes from this region are from NH tropical Africa, with African CH$_4$ emissions increasing
from $5 \, TgCH_4 \, yr^{-1}$ at 20 ka BP to some $26 \, TgCH_4 \, yr^{-1}$ between 13 and 8.5 ka BP, with emissions subsequently decreasing
gradually to $8 \, TgCH_4 \, yr^{-1}$ after 2 ka BP. In comparison to these fluxes from NH Africa, fluxes from NH tropical Asia and
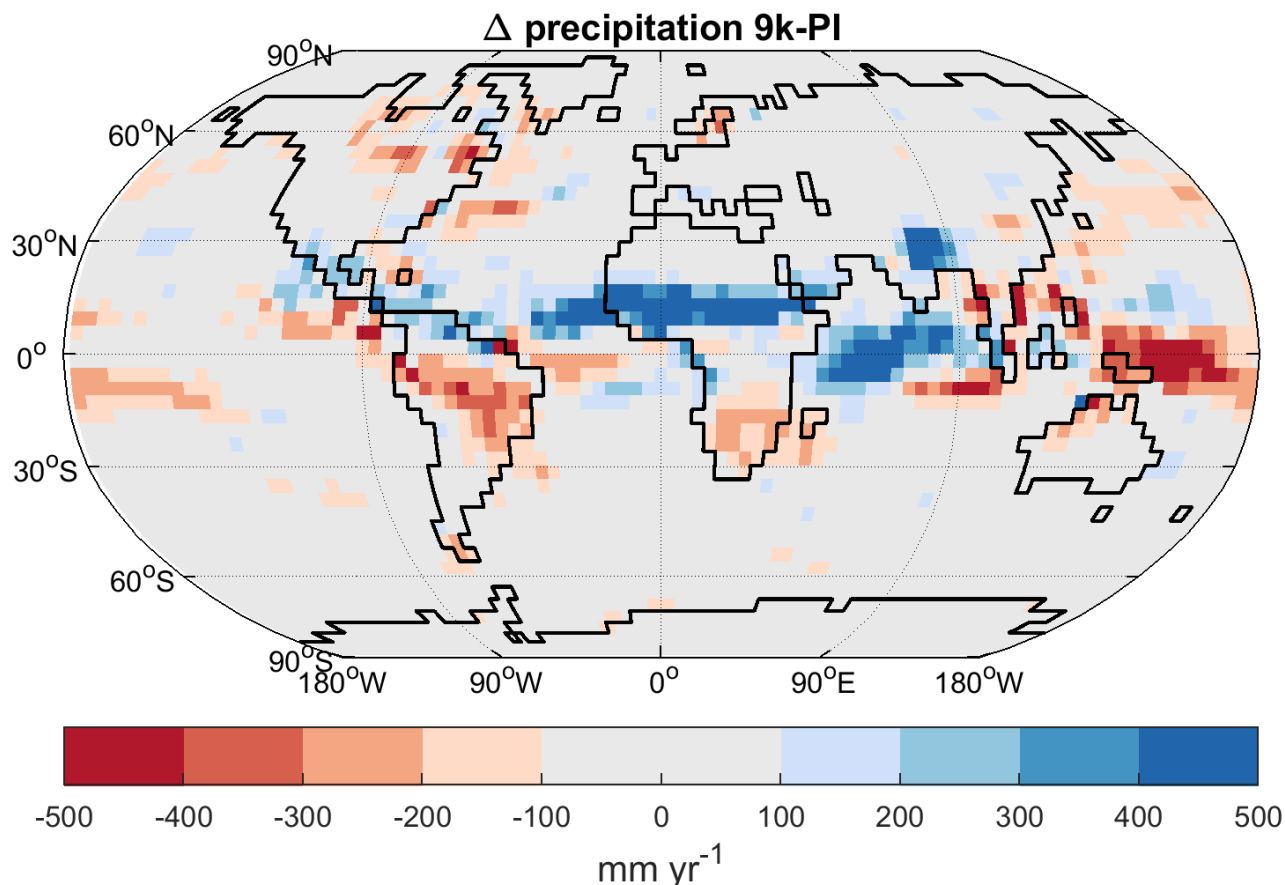
Figure 10. Precipitation change 9 ka BP - PI, continental outline is from 9 ka BP.

America change very little, except for the rapid changes in fluxes from NH tropical Asia connected to AMOC changes after
355 MWP1a in the *base* and during the Younger Dryas in the *MWM* experiment.

Finally, focusing on the Holocene changes after 8 ka BP, we see a decreasing trend in emissions from the NH tropics
(Fig. 11a), while emissions from the SH tropics increase. The latter increase is due to a generally increasing trend in precip-
itation over South America (Fig. 10), leading to increasing emissions from the Amazon region, while the former is due to a
decreasing trend in precipitation over NH tropical regions, mainly in Africa, but also over northern India. These precipitation
360 trends are ultimately caused by orbital changes with the change in precession leading to a decrease in radiation reaching NH
tropical areas and an increase in radiation reaching SH tropical areas, causing changes in land-sea temperature contrasts and
thus changes in monsoon circulation and related precipitation (Dallmeyer et al., 2021). We thus see a very similar trend to
Singarayer et al. (2011), who saw decreasing emissions from the NH tropics and increasing emissions from the SH over the
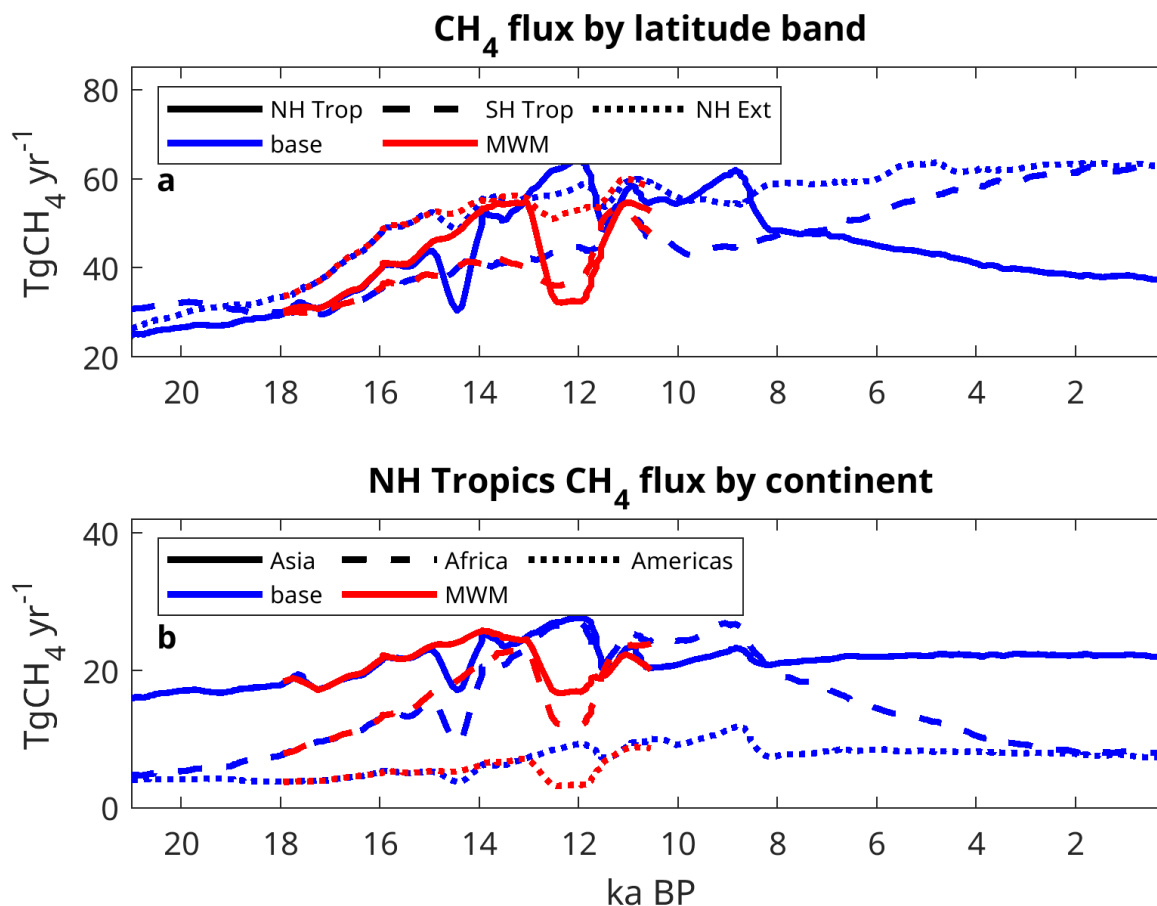
Figure 11. Net CH$_4$ flux over time by latitude band (a), and by continent (b) for the NH tropics (0-30°N).

last 8 ka. Singarayer et al. (2011) were thus able to explain the Holocene trend in reconstructed CH$_4$, a decrease from early
365 to mid Holocene, followed by an increase from mid to late Holocene. In our model, however, these trends more or less cancel
each other, thus leading to very small changes in overall methane emissions, despite the substantial changes in regional fluxes.

4 Discussion

Our present publication generally confirms the results from time-slice experiments we obtained earlier (Kleinen et al., 2020),
however importantly integrating a methane sink component into the modelling system and enabling the investigation of highly
370 transient changes in methane as during the BA-YD transition. Thus we corroborate that the large-scale change in atmospheric
methane from LGM to Holocene is mainly due to changes in wetland emissions, with the tropical areas being the main emitting
region, while NH extratropics play a secondary role. This change in wetland emissions can be attributed to increases in soil

carbon storage, increases in atmospheric CO_2 and further climate changes, with warming playing the most prominent role (Kleinen et al., 2020). While there is a number of uncertain parameters in the wetland methane emission model, changes in

375 these tend to have very similar effects in both LGM and PI climate states, proportionally adjusting the emission strengths so that their LGM to PI ratio remains little affected. The latter is instead determined by the changes in soil C, atmospheric CO_2 and climate. Therefore factors like CO_2 fertilisation, the increase in vegetation productivity with increasing atmospheric CO_2, would need to be adjusted in order to affect the ratio of LGM to PI CH_4 emissions. As the difference in terrestrial carbon storage between LGM and PI is on the high side (Jeltsch-Thömmes et al. (2019), for example, estimate 450 to 1250 PgC for

380 the LGM to PI change in terrestrial C, including substantial C stores like peatlands which we do not consider in our model), a decrease in CO_2 sensitivity might improve overall results.

We calibrated the contributions by the different methane sources to the total flux to be conformal to the present-day source distribution (Saunois et al., 2016, 2020), and the relative contributions of the single sources to the total emissions change very little over the course of the deglaciation. In terms of total emissions, Valdes et al. (2005) assume LGM emissions of

385 $152.4\,Tg CH_4\,yr^{-1}$ and PI emissions of $198.9\,Tg CH_4\,yr^{-1}$, while Hopcroft et al. (2017) obtain $129.7\,Tg CH_4\,yr^{-1}$ at LGM and $197.2\,Tg CH_4\,yr^{-1}$ at PI. Both of these estimates are higher than our results (net emissions of $90\,Tg CH_4 yr^{-1}$ at 20 ka BP and $165\,Tg CH_4 yr^{-1}$ at PI), requiring a shorter atmospheric lifetime of CH_4 than we obtain.

Both Valdes et al. (2005) and Hopcroft et al. (2017) assume oceanic CH_4 emissions, with LGM emissions of the order of $11\,Tg CH_4\,yr^{-1}$ and PI emissions of the order of $14\,Tg CH_4\,yr^{-1}$. Our assumption is that the oceanic emissions need to be

390 subsumed under the geological emissions (Etiope, 2015; Saunois et al., 2016, 2020), the total amount of which is highly debated at present, with direct measurements showing substantially higher estimates (Etiope, 2015; Mazzini et al., 2021) than ice-core based reconstructions of emissions during the YD (Petrenko et al., 2017) or PI (Hmiel et al., 2020). We chose geological emissions of $5\,Tg CH_4\,yr^{-1}$, the maximum still compatible with ice-core measurements. Assuming geological emissions of $60\,Tg CH_4\,yr^{-1}$, more in line with Saunois et al. (2016), would make it extremely difficult to match the LGM methane budget,

395 as geological emissions would then make up more than half the possible emissions, requiring even larger decreases in all other methane fluxes.

For methane emissions from herbivorous mammals, this source category is at present dominated by domesticated animals, mainly cows, and both the densities and the species distributions of wild herbivorous mammals in an Earth System untouched by humans, as we assume it to be for the LGM state, is completely unknown. We thus tied the emissions by herbivorous

400 mammals to the net primary production as a proxy for food availability. Previous estimates (Crutzen et al., 1986; Chappellaz et al., 1993) were derived using a different methodology, estimating key species populations and extrapolating emissions from these. Chappellaz et al. (1993) thus estimate herbivore emissions of $15\,Tg CH_4\,yr^{-1}$ for the Preindustrial Holocene and of $20\,Tg CH_4\,yr^{-1}$ for the LGM, arguing that grasslands expanded by 50% at LGM, thus enlarging the habitat. In our model experiments, however, we find that grasslands do not expand at the LGM in comparison to PI. Instead, grasslands are slightly

405 larger in the PI state than at LGM. It may be that the discrepancy in areal estimates is due to Chappellaz et al. (1993) assuming grassland in LGM eastern Siberia, but our model instead finds that polar deserts expand in there due to extremely dry conditions. Other estimates of herbivore emissions generally go back to the estimate by Crutzen et al. (1986), which also forms the basis

for the Chappellaz et al. (1993) estimate, and thus do not need to be discussed here further. Smith et al. (2016), however, also estimated Late Pleistocene and Preindustrial methane production form herbivorous mammals. They estimate herbivore

410 emissions of $150\,TgCH_4\,yr^{-1}$ for the late Pleistocene, which is slightly less than double our estimate of net total emissions at LGM. Thus their estimate would require a dramatically shorter lifetime for atmospheric CH_4 than for the PI state, which is considered incompatible with present-day understanding of the methane cycle (Murray et al., 2014; Hopcroft et al., 2017).

Finally, the mid-Holocene decrease in atmospheric methane is the one aspect of the development of atmospheric methane in the time from LGM to PI that we were unable to reproduce in a satisfactory way. Singarayer et al. (2011) were able to

415 attribute these changes to the orbital forcing. They found that due to precession-caused insolation changes, wetland emissions from the SH tropics increase after 5 ka BP, while the emissions from the NH tropics decrease, with the NH decrease being smaller than the SH increase after 5 ka BP. We see a very similar behaviour in our model: wetland emissions from the NH tropics, especially from Africa, decrease after 8 ka BP, while emissions from the SH tropics, predominantly the Amazon region, increase (Fig. 11). The net result in our case, though, is that the NH decrease is exactly compensated by the SH increase, thus

420 leading to no change in total emissions. Our model thus produces constant emissions from 8 ka BP to PI, leading to a constant atmospheric concentration with neither a decrease before 5 ka BP nor an increase after 5 ka BP being apparent. We suspect that this behaviour may be due either to NH extratropical emissions or to the monsoon changes in north Africa. The total NH extratropical emissions are rather stable over the course of the Holocene (Fig. 11), despite large regional changes (Fig. 9), as changes in one region are compensated by changes in other regions. On the other hand, the expansion of the African monsoon

425 system in our model is relatively limited in comparison to reconstructions. The latter show an expansion of the monsoon into the Sahara, while we only get an increase in the Sahel. The larger extent in the reconstructions would imply a different temporal behaviour with a narrower emission peak. With this change in African emissions, the emission decrease from the NH tropics would be less than the emission increase from the SH tropics, thus leading to the methane trajectory observed in ice cores.

5 Conclusions

430 Our model experiments demonstrate for the first time how the complete methane cycle changes over the course of the deglaciation. We found that the atmospheric lifetime of CH_4 has increased slightly, from $10.4\,yrs$ at 18 ka BP to a maximum of $12\,yrs$ at 12 ka BP, implying that the observed doubling of the atmospheric CH_4 concentration during this interval has to be explained primarily by changes in CH_4 emissions. The model is capable of simulating such changes in CH_4 sources, with wetland emissions increasing from $80\,TgCH_4\,yr^{-1}$ to $150\,TgCH_4\,yr^{-1}$ primarily driven by increases in vegetation productivity. We are able

435 to reproduce all major features of the deglacial ice-core methane record, with the exception of the mid-Holocene decrease in methane, when a decrease in NH methane sources is perfectly compensated by an increase in SH sources. For much of the deglaciation, our atmospheric transport model reproduces both Antarctic and Greenland methane records, thus also capturing the interhemispheric gradient.

We also are able to simulate significant emissions of CH_4 from shelf areas which were flooded in the course of the deglacia-
tion. Simulated changes in total terrestrial carbon storage of ca. 710 GtC increase from LGM to PI are at the upper end of
modelling estimates.

Some of the abrupt deglacial methane changes, however, cannot be reproduced spontaneously, but rather require dedicated
model setups: As shown in our *base* experiment (and by Kapsch et al. (2022)), a simple application of meltwater input time-
series from ice sheet reconstructions will not lead to climate changes as reconstructed from proxy data. The meltwater input
from MWP 1a leads to a collapse of the North Atlantic AMOC circulation, leading to a strong cooling event in circum-
Atlantic areas at the time when the Bølling-Allerød warming would rather be expected. With appropriate management of the
ice sheet meltwater, however, we were able to reproduce the entire deglaciation sequence in experiment *MWM*. Thus storing
the meltwater from the Laurentide ice sheet and releasing the accumulated meltwater at 12.8 ka BP leads to an sequence of
Bølling-Allerød warming, Younger Dryas cooling, and Preboreal warming that is, in terms of atmospheric methane, very close
to ice core records from Antarctica and Greenland.

Code and data availability. The primary data, i.e. the model code for MPI-ESM, are freely available to the scientific commu- nity and can be
accessed with a license on the MPI-M model distri- bution website http://www.mpimet.mpg.de/en/science/models (last access: 29 September
2022). In addition, secondary data and scripts that may be useful in reproducing the authors' work are archived by the Max Planck Institute
for Meteorology. They can be obtained by contacting the first author or publications@mpimet.mpg.de.

Author contributions. TK: Model development, experiment design and analysis, main author of text. SG: Atmospheric sink development,
interpretation of results. BS: Atmospheric sink, interpretation of results. VB: Experiment interpretation. All: Discussion of results, editing of
manuscript.

Competing interests. None.

Acknowledgements. We thank Anne Dallmeyer for comments on an earlier version of this manuscript. We acknowledge support through the
project Palmod, funded by the German Federal Ministry of Education and Research (BMBF), Grant Nos. 01LP1921A and 01LP1921B. This
work used resources of the Deutsches Klimarechenzentrum (DKRZ) granted by its Scientific Steering Committee (WLA) under Project ID
bm1030.

References

Amante, C. and Eakins, B.: ETOPO1 1 Arc-Minute Global Relief Model: Procedures, Data Sources and Analysis, NOAA technical memorandum NESDIS NGDC-24, National Geophysical Data Center, NOAA, https://doi.org/10.7289/V5C8276M, 2009.

Berger, A. L.: Long-Term Variations of Daily Insolation and Quaternary Climatic Changes, Journal of Atmospheric Science, 35, 2362–2367, https://doi.org/10.1175/1520-0469(1978)035<2362:LTVODI>2.0.CO;2, 1978.

Beven, K. J. and Kirkby, M. J.: A physically based, variable contributing area model of basin hydrology, Hydrological Sciences Bulletin, 24, 43–69, 1979.

Bousquet, P., Ringeval, B., Pison, I., Dlugokencky, E. J., Brunke, E.-G., Carouge, C., Chevallier, F., Fortems-Cheiney, A., Frankenberg, C., Hauglustaine, D. A., Krummel, P. B., Langenfelds, R. L., Ramonet, M., Schmidt, M., Steele, L. P., Szopa, S., Yver, C., Viovy, N., and Ciais, P.: Source attribution of the changes in atmospheric methane for 2006–2008, Atmospheric Chemistry and Physics, 11, 3689–3700, https://doi.org/10.5194/acp-11-3689-2011, 2011.

Briggs, R. D., Pollard, D., and Tarasov, L.: A data-constrained large ensemble analysis of Antarctic evolution since the Eemian, Quaternary Science Reviews, 103, 91 – 115, https://doi.org/10.1016/j.quascirev.2014.09.003, 2014.

Buytaert, W.: Topmodel, http://cran.r-project.org/web/packages/topmodel/index.html, accessed: 21 December 2016, 2011.

Chappellaz, J., Stowasser, C., Blunier, T., Baslev-Clausen, D., Brook, E. J., Dallmayr, R., Faïn, X., Lee, J. E., Mitchell, L. E., Pascual, O., Romanini, D., Rosen, J., and Schüpbach, S.: High-resolution glacial and deglacial record of atmospheric methane by continuous-flow and laser spectrometer analysis along the NEEM ice core, Climate of the Past, 9, 2579–2593, https://doi.org/10.5194/cp-9-2579-2013, 2013.

Chappellaz, J. A., Fung, I. Y., and Thompson, A. M.: The atmospheric CH_4 increase since the Last Glacial Maximum: (1). Source estimates, Tellus B: Chemical and Physical Meteorology, 45, 228–241, https://doi.org/10.3402/tellusb.v45i3.15726, 1993.

Clauss, M., Dittmann, M. T., Vendl, C., Hagen, K. B., Frei, S., Ortmann, S., Müller, D. W. H., Hammer, S., Munn, A. J., Schwarm, A., and Kreuzer, M.: Review: Comparative methane production in mammalian herbivores, Animal, 14, s113–s123, https://doi.org/10.1017/S1751731119003161, 2020.

Crutzen, P. J., Aselmann, I., and Seiler, W.: Methane production by domestic animals, wild ruminants, other herbivorous fauna, and humans, Tellus B: Chemical and Physical Meteorology, 38, 271–284, https://doi.org/10.3402/tellusb.v38i3-4.15135, 1986.

Dallmeyer, A., Claussen, M., Lorenz, S. J., and Shanahan, T.: The end of the African humid period as seen by a transient comprehensive Earth system model simulation of the last 8000 years, Climate of the Past, 16, 117–140, https://doi.org/10.5194/cp-16-117-2020, 2020.

Dallmeyer, A., Claussen, M., Lorenz, S. J., Sigl, M., Toohey, M., and Herzschuh, U.: Holocene vegetation transitions and their climatic drivers in MPI-ESM1.2, Climate of the Past, 17, 2481–2513, https://doi.org/10.5194/cp-17-2481-2021, 2021.

Dallmeyer, A., Kleinen, T., Claussen, M., Weitzel, N., Cao, X., and Herzschuh, U.: The deglacial forest conundrum, Nature Communications in press, 2022.

Etiope, G.: Gas Seepage Classification and Global Distribution, pp. 17–43, Springer International Publishing, Cham, https://doi.org/10.1007/978-3-319-14601-0_2, 2015.

Eyring, V., Bony, S., Meehl, G. A., Senior, C. A., Stevens, B., Stouffer, R. J., and Taylor, K. E.: Overview of the Coupled Model Intercomparison Project Phase 6 (CMIP6) experimental design and organization, Geoscientific Model Development, 9, 1937–1958, https://doi.org/10.5194/gmd-9-1937-2016, 2016.

Fischer, H., Behrens, M., Bock, M., Richter, U., Schmitt, J., Loulergue, L., Chappellaz, J., Spahni, R., Blunier, T., Leuenberger, M., and Stocker, T. F.: Changing boreal methane sources and constant biomass burning during the last termination, Nature, 452, 864–867, 500 https://doi.org/10.1038/nature06825, 2008.

Goll, D. S., Brovkin, V., Liski, J., Raddatz, T., Thum, T., and Todd-Brown, K. E. O.: Strong dependence of CO_2 emissions from anthropogenic land cover change on initial land cover and soil carbon parametrization, Global Biogeochemical Cycles, 29, 1511–1523, https://doi.org/10.1002/2014GB004988, 2015.

Gromov, S., Steil, B., Kleinen, T., and Brovkin, V.: On the factors controlling the atmospheric oxidative capacity and CH_4 lifetime during 505 the LGM, Geophysical Research Abstracts, 20, 19 038–1, https://doi.org/10.13140/RG.2.2.20300.23682, 2018.

Guenther, A. B., Jiang, X., Heald, C. L., Sakulyanontvittaya, T., Duhl, T., Emmons, L. K., and Wang, X.: The Model of Emissions of Gases and Aerosols from Nature version 2.1 (MEGAN2.1): an extended and updated framework for modeling biogenic emissions, Geoscientific Model Development, 5, 1471–1492, https://doi.org/10.5194/gmd-5-1471-2012, 2012.

Hmiel, B., Petrenko, V. V., Dyonisius, M. N., Buizert, C., Smith, A. M., Place, P. F., Harth, C., Beaudette, R., Hua, Q., Yang, B., Vimont, I., 510 Michel, S. E., Severinghaus, J. P., Etheridge, D., Bromley, T., Schmitt, J., Faïn, X., Weiss, R. F., and Dlugokencky, E.: Preindustrial $^{14}CH_4$ indicates greater anthropogenic fossil CH_4 emissions, Nature, 578, 409–412, https://doi.org/10.1038/s41586-020-1991-8, 2020.

Hopcroft, P. O., Valdes, P. J., O'Connor, F. M., Kaplan, J. O., and Beerling, D. J.: Understanding the glacial methane cycle, Nature Communications, 8, 14 383, https://doi.org/10.1038/ncomms14383, 2017.

Hristov, A. N.: Historic, pre-European settlement, and present-day contribution of wild ruminants to enteric methane emissions in the United 515 States, Journal of Animal Science, 90, 1371–1375, https://doi.org/10.2527/jas.2011-4539, 2012.

Ivanovic, R. F., Gregoire, L. J., Kageyama, M., Roche, D. M., Valdes, P. J., Burke, A., Drummond, R., Peltier, W. R., and Tarasov, L.: Transient climate simulations of the deglaciation 21–9 thousand years before present (version 1) – PMIP4 Core experiment design and boundary conditions, Geoscientific Model Development, 9, 2563–2587, https://doi.org/10.5194/gmd-9-2563-2016, 2016.

Jeltsch-Thömmes, A., Battaglia, G., Cartapanis, O., Jaccard, S. L., and Joos, F.: Low terrestrial carbon storage at the Last Glacial Maximum: 520 constraints from multi-proxy data, Climate of the Past, 15, 849–879, https://doi.org/10.5194/cp-15-849-2019, 2019.

Joeckel, P., Kerkweg, A., Pozzer, A., Sander, R., Tost, H., Riede, H., Baumgaertner, A., Gromov, S., and Kern, B.: Development cycle 2 of the Modular Earth Submodel System (MESSy2), Geoscientific Model Development, 3, 717–752, https://doi.org/10.5194/gmd-3-717-2010, 2010.

Kaiser, J. W., Heil, A., Andreae, M. O., Benedetti, A., Chubarova, N., Jones, L., Morcrette, J.-J., Razinger, M., Schultz, M. G., Suttie, M., 525 and van der Werf, G. R.: Biomass burning emissions estimated with a global fire assimilation system based on observed fire radiative power, Biogeosciences, 9, 527–554, https://doi.org/10.5194/bg-9-527-2012, 2012.

Kapsch, M.-L., Mikolajewicz, U., Ziemen, F., and Schannwell, C.: Ocean Response in Transient Simulations of the Last Deglaciation Dominated by Underlying Ice-Sheet Reconstruction and Method of Meltwater Distribution, Geophysical Research Letters, 49, e2021GL096 767, https://doi.org/10.1029/2021GL096767, 2022.

530 Kinne, S., O'Donnel, D., Stier, P., Kloster, S., Zhang, K., Schmidt, H., Rast, S., Giorgetta, M., Eck, T. F., and Stevens, B.: MAC-v1: A new global aerosol climatology for climate studies, Journal of Advances in Modeling Earth Systems, 5, 704–740, https://doi.org/10.1002/jame.20035, 2013.

Kirschke, S., Bousquet, P., Ciais, P., Saunois, M., Canadell, J. G., Dlugokencky, E. J., Bergamaschi, P., Bergmann, D., Blake, D. R., Bruhwiler, L., Cameron-Smith, P., Castaldi, S., Chevallier, F., Feng, L., Fraser, A., Heimann, M., Hodson, E. L., Houweling, S., Josse, B., Fraser, P. J., 535 Krummel, P. B., Lamarque, J.-F., Langenfelds, R. L., Le Quere, C., Naik, V., O'Doherty, S., Palmer, P. I., Pison, I., Plummer, D., Poulter,

B., Prinn, R. G., Rigby, M., Ringeval, B., Santini, M., Schmidt, M., Shindell, D. T., Simpson, I. J., Spahni, R., Steele, L. P., Strode, S. A., Sudo, K., Szopa, S., van der Werf, G. R., Voulgarakis, A., van Weele, M., Weiss, R. F., Williams, J. E., and Zeng, G.: Three decades of global methane sources and sinks, Nature Geosci, 6, 813–823, 2013.

Klein Goldewijk, K., Beusen, A., Doelman, J., and Stehfest, E.: Anthropogenic land use estimates for the Holocene – HYDE 3.2, Earth System Science Data, 9, 927–953, https://doi.org/10.5194/essd-9-927-2017, 2017.

Kleinen, T., Mikolajewicz, U., and Brovkin, V.: Terrestrial methane emissions from the Last Glacial Maximum to the preindustrial period, Climate of the Past, 16, 575–595, https://doi.org/10.5194/cp-16-575-2020, 2020.

Kleinen, T., Gromov, S., Steil, B., and Brovkin, V.: Atmospheric methane underestimated in future climate projections, Environmental Research Letters, 16, 094 006, https://doi.org/10.1088/1748-9326/ac1814, 2021.

Köhler, P., Nehrbass-Ahles, C., Schmitt, J., Stocker, T. F., and Fischer, H.: A 156 kyr smoothed history of the atmospheric greenhouse gases CO_2, CH_4, and N_2O and their radiative forcing, Earth System Science Data, 9, 363–387, https://doi.org/10.5194/essd-9-363-2017, 2017.

Lambeck, K., Rouby, H., Purcell, A., Sun, Y., and Sambridge, M.: Sea level and global ice volumes from the Last Glacial Maximum to the Holocene, Proceedings of the National Academy of Sciences, 111, 15 296–15 303, https://doi.org/10.1073/pnas.1411762111, 2014.

Lasslop, G., Thonicke, K., and Kloster, S.: SPITFIRE within the MPI Earth system model: Model development and evaluation, Journal of Advances in Modeling Earth Systems, 6, 740–755, https://doi.org/10.1002/2013MS000284, 2014.

Lee, J. E., Edwards, J. S., Schmitt, J., Fischer, H., Bock, M., and Brook, E. J.: Excess methane in Greenland ice cores associated with high dust concentrations, Geochimica et Cosmochimica Acta, 270, 409–430, https://doi.org/10.1016/j.gca.2019.11.020, 2020.

Marthews, T. R., Dadson, S. J., Lehner, B., Abele, S., and Gedney, N.: High-resolution global topographic index values for use in large-scale hydrological modelling, Hydrology and Earth System Sciences, 19, 91–104, https://doi.org/10.5194/hess-19-91-2015, 2015.

Mauritsen, T., Bader, J., Becker, T., Behrens, J., Bittner, M., Brokopf, R., Brovkin, V., Claussen, M., Crueger, T., Esch, M., Fast, I., Fiedler, S., Fläschner, D., Gayler, V., Giorgetta, M., Goll, D. S., Haak, H., Hagemann, S., Hedemann, C., Hohenegger, C., Ilyina, T., Jahns, T., Jimenéz-de-la Cuesta, D., Jungclaus, J., Kleinen, T., Kloster, S., Kracher, D., Kinne, S., Kleberg, D., Lasslop, G., Kornblueh, L., Marotzke, J., Matei, D., Meraner, K., Mikolajewicz, U., Modali, K., Möbis, B., Müller, W. A., Nabel, J. E. M. S., Nam, C. C. W., Notz, D., Nyawira, S.-S., Paulsen, H., Peters, K., Pincus, R., Pohlmann, H., Pongratz, J., Popp, M., Raddatz, T. J., Rast, S., Redler, R., Reick, C. H., Rohrschneider, T., Schemann, V., Schmidt, H., Schnur, R., Schulzweida, U., Six, K. D., Stein, L., Stemmler, I., Stevens, B., von Storch, J.-S., Tian, F., Voigt, A., Vrese, P., Wieners, K.-H., Wilkenskjeld, S., Winkler, A., and Roeckner, E.: Developments in the MPI-M Earth System Model version 1.2 (MPI-ESM1.2) and its response to increasing CO_2, Journal of Advances in Modeling Earth Systems, 11, 998–1038, https://doi.org/10.1029/2018MS001400, 2019.

Mazzini, A., Sciarra, A., Etiope, G., Sadavarte, P., Houweling, S., Pandey, S., and Husein, A.: Relevant methane emission to the atmosphere from a geological gas manifestation, Scientific Reports, 11, 4138, https://doi.org/10.1038/s41598-021-83369-9, 2021.

McManus, J. F., Francois, R., Gherardi, J.-M., Keigwin, L. D., and Brown-Leger, S.: Collapse and rapid resumption of Atlantic meridional circulation linked to deglacial climate changes, Nature, 428, 834–837, https://doi.org/10.1038/nature02494, 2004.

Meccia, V. L. and Mikolajewicz, U.: Interactive ocean bathymetry and coastlines for simulating the last deglaciation with the Max Planck Institute Earth System Model (MPI-ESM-v1.2), Geoscientific Model Development, 11, 4677–4692, https://doi.org/10.5194/gmd-11-4677-2018, 2018.

Mikolajewicz, U., Ziemen, F., Cioni, G., Claussen, M., Fraedrich, K., Heidkamp, M., Hohenegger, C., Jimenez de la Cuesta, D., Kapsch, M.-L., Lemburg, A., Mauritsen, T., Meraner, K., Röber, N., Schmidt, H., Six, K. D., Stemmler, I., Tamarin-Brodsky, T., Winkler, A., Zhu,

X., and Stevens, B.: The climate of a retrograde rotating Earth, Earth System Dynamics, 9, 1191–1215, https://doi.org/10.5194/esd-9-1191-2018, 2018.

575 Murray, L. T., Mickley, L. J., Kaplan, J. O., Sofen, E. D., Pfeiffer, M., and Alexander, B.: Factors controlling variability in the oxidative capacity of the troposphere since the Last Glacial Maximum, Atmospheric Chemistry and Physics, 14, 3589–3622, https://doi.org/10.5194/acp-14-3589-2014, 2014.

Murton, J. B., Bateman, M. D., Dallimore, S. R., Teller, J. T., and Yang, Z.: Identification of Younger Dryas outburst flood path from Lake Agassiz to the Arctic Ocean, Nature, 464, 740–743, https://doi.org/10.1038/nature08954, 2010.

580 Petit, J. R., Jouzel, J., Raynaud, D., Barkov, N. I., Barnola, J.-M., Basile, I., Bender, M., Chappellaz, J., Davis, M., Delaygue, G., Delmotte, M., Kotlyakov, V. M., Legrand, M., Lipenkov, V. Y., Lorius, C., Pépin, L., Ritz, C., Saltzman, E., and Stievenard, M.: Climate and atmospheric history of the past 420,000 years from the Vostok ice core, Antarctica, Nature, 399, 429–436, https://doi.org/10.1038/20859, 1999.

Petrenko, V. V., Smith, A. M., Schaefer, H., Riedel, K., Brook, E., Baggenstos, D., Harth, C., Hua, Q., Buizert, C., Schilt, A., Fain, X., 585 Mitchell, L., Bauska, T., Orsi, A., Weiss, R. F., and Severinghaus, J. P.: Minimal geological methane emissions during the Younger Dryas–Preboreal abrupt warming event, Nature, 548, 443–446, 2017.

Price, C. and Rind, D.: A simple lightning parameterization for calculating global lightning distributions, Journal of Geophysical Research: Atmospheres, 97, 9919–9933, https://doi.org/10.1029/92JD00719, 1992.

Price, C. and Rind, D.: What determines the cloud-to-ground lightning fraction in thunderstorms?, Geophysical Research Letters, 20, 463– 590 466, https://doi.org/10.1029/93GL00226, 1993.

Prigent, C., Papa, F., Aires, F., Jimenez, C., Rossow, W. B., and Matthews, E.: Changes in land surface water dynamics since the 1990s and relation to population pressure, Geophysical Research Letters, 39, L08 403, https://doi.org/10.1029/2012GL051276, 2012.

Reick, C. H., Gayler, V., Goll, D., Hagemann, S., Heidkamp, M., Nabel, J. E., Raddatz, T., Roeckner, E., Schnur, R., and Wilkenskjeld, S.: JSBACH 3 - The land component of the MPI Earth System Model: documentation of version 3.2, Tech. Rep. Berichte zur Erdsystem-595 forschung 240, Max-Planck Institut für Meteorologie, Hamburg, Germany, https://doi.org/10.17617/2.3279802, 2021.

Rhodes, R. H., Faïn, X., Stowasser, C., Blunier, T., Chappellaz, J., McConnell, J. R., Romanini, D., Mitchell, L. E., and Brook, E. J.: Continuous methane measurements from a late Holocene Greenland ice core: Atmospheric and in-situ signals, Earth and Planetary Science Letters, 368, 9–19, https://doi.org/10.1016/j.epsl.2013.02.034, 2013.

Riddick, T., Brovkin, V., Hagemann, S., and Mikolajewicz, U.: Dynamic hydrological discharge modelling for coupled climate model 600 simulations of the last glacial cycle: the MPI-DynamicHD model version 3.0, Geoscientific Model Development, 11, 4291–4316, https://doi.org/10.5194/gmd-11-4291-2018, 2018.

Riley, W. J., Subin, Z. M., Lawrence, D. M., Swenson, S. C., Torn, M. S., Meng, L., Mahowald, N. M., and Hess, P.: Barriers to predicting changes in global terrestrial methane fluxes: analyses using CLM4Me, a methane biogeochemistry model integrated in CESM, Biogeosciences, 8, 1925–1953, https://doi.org/10.5194/bg-8-1925-2011, 2011.

605 Saunois, M., Bousquet, P., Poulter, B., Peregon, A., Ciais, P., Canadell, J. G., Dlugokencky, E. J., Etiope, G., Bastviken, D., Houweling, S., Janssens-Maenhout, G., Tubiello, F. N., Castaldi, S., Jackson, R. B., Alexe, M., Arora, V. K., Beerling, D. J., Bergamaschi, P., Blake, D. R., Brailsford, G., Brovkin, V., Bruhwiler, L., Crevoisier, C., Crill, P., Covey, K., Curry, C., Frankenberg, C., Gedney, N., Höglund-Isaksson, L., Ishizawa, M., Ito, A., Joos, F., Kim, H.-S., Kleinen, T., Krummel, P., Lamarque, J.-F., Langenfelds, R., Locatelli, R., Machida, T., Maksyutov, S., McDonald, K. C., Marshall, J., Melton, J. R., Morino, I., Naik, V., O'Doherty, S., Parmentier, F.-J. W., Patra, P. K., Peng, 610 C., Peng, S., Peters, G. P., Pison, I., Prigent, C., Prinn, R., Ramonet, M., Riley, W. J., Saito, M., Santini, M., Schroeder, R., Simpson, I. J.,

Spahni, R., Steele, P., Takizawa, A., Thornton, B. F., Tian, H., Tohjima, Y., Viovy, N., Voulgarakis, A., van Weele, M., van der Werf, G. R., Weiss, R., Wiedinmyer, C., Wilton, D. J., Wiltshire, A., Worthy, D., Wunch, D., Xu, X., Yoshida, Y., Zhang, B., Zhang, Z., and Zhu, Q.: The global methane budget 2000–2012, Earth System Science Data, 8, 697–751, https://doi.org/10.5194/essd-8-697-2016, 2016.

Saunois, M., Stavert, A. R., Poulter, B., Bousquet, P., Canadell, J. G., Jackson, R. B., Raymond, P. A., Dlugokencky, E. J., Houweling, S.,
615   Patra, P. K., Ciais, P., Arora, V. K., Bastviken, D., Bergamaschi, P., Blake, D. R., Brailsford, G., Bruhwiler, L., Carlson, K. M., Carrol, M., Castaldi, S., Chandra, N., Crevoisier, C., Crill, P. M., Covey, K., Curry, C. L., Etiope, G., Frankenberg, C., Gedney, N., Hegglin, M. I., Höglund-Isaksson, L., Hugelius, G., Ishizawa, M., Ito, A., Janssens-Maenhout, G., Jensen, K. M., Joos, F., Kleinen, T., Krummel, P. B., Langenfelds, R. L., Laruelle, G. G., Liu, L., Machida, T., Maksyutov, S., McDonald, K. C., McNorton, J., Miller, P. A., Melton, J. R., Morino, I., Müller, J., Murguia-Flores, F., Naik, V., Niwa, Y., Noce, S., O'Doherty, S., Parker, R. J., Peng, C., Peng, S., Peters, G. P.,
620   Prigent, C., Prinn, R., Ramonet, M., Regnier, P., Riley, W. J., Rosentreter, J. A., Segers, A., Simpson, I. J., Shi, H., Smith, S. J., Steele, L. P., Thornton, B. F., Tian, H., Tohjima, Y., Tubiello, F. N., Tsuruta, A., Viovy, N., Voulgarakis, A., Weber, T. S., van Weele, M., van der Werf, G. R., Weiss, R. F., Worthy, D., Wunch, D., Yin, Y., Yoshida, Y., Zhang, W., Zhang, Z., Zhao, Y., Zheng, B., Zhu, Q., Zhu, Q., and Zhuang, Q.: The Global Methane Budget 2000–2017, Earth System Science Data, 12, 1561–1623, https://doi.org/10.5194/essd-12-1561-2020, 2020.

625 Schaffer, J., Timmermann, R., Arndt, J. E., Kristensen, S. S., Mayer, C., Morlighem, M., and Steinhage, D.: A global, high-resolution data set of ice sheet topography, cavity geometry, and ocean bathymetry, Earth System Science Data, 8, 543–557, https://doi.org/10.5194/essd-8-543-2016, 2016.

Schneck, R., Reick, C. H., and Raddatz, T.: Land contribution to natural CO_2 variability on time scales of centuries, Journal of Advances in Modeling Earth Systems, 5, 354–365, https://doi.org/10.1002/jame.20029, 2013.

630 Singarayer, J. S., Valdes, P. J., Friedlingstein, P., Nelson, S., and Beerling, D. J.: Late Holocene methane rise caused by orbitally controlled increase in tropical sources, Nature, 470, 82–85, https://doi.org/10.1038/nature09739, 2011.

Smith, F. A., Hammond, J. I., Balk, M. A., Elliott, S. M., Lyons, S. K., Pardi, M. I., Tomé, C. P., Wagner, P. J., and Westover, M. L.: Exploring the influence of ancient and historic megaherbivore extirpations on the global methane budget, Proceedings of the National Academy of Sciences, 113, 874–879, https://doi.org/10.1073/pnas.1502547112, 2016.

635 Stanford, J., Rohling, E., Bacon, S., Roberts, A., Grousset, F., and Bolshaw, M.: A new concept for the paleoceanographic evolution of Heinrich event 1 in the North Atlantic, Quaternary Science Reviews, 30, 1047–1066, https://doi.org/10.1016/j.quascirev.2011.02.003, 2011.

Tarasov, L., Dyke, A. S., Neal, R. M., and Peltier, W.: A data-calibrated distribution of deglacial chronologies for the North American ice complex from glaciological modeling, Earth and Planetary Science Letters, 315-316, 30 – 40, https://doi.org/10.1016/j.epsl.2011.09.010,
640   2012.

Thompson, A. M., Chappellaz, J. A., Fung, I. Y., and Kucsera, T. L.: The atmospheric CH_4 increase since the Last Glacial Maximum: (2). interactions with oxidants, Tellus, Series B, 45, 242–257, https://doi.org/10.1034/j.1600-0889.1993.t01-2-00003.x, 1993.

Valdes, P. J., Beerling, D. J., and Johnson, C. E.: The ice age methane budget, Geophys. Res. Lett., 32, L02 704, https://doi.org/10.1029/2004GL021004, 2005.

645 Wania, R., Ross, I., and Prentice, I. C.: Implementation and evaluation of a new methane model within a dynamic global vegetation model: LPJ-WHyMe v1.3.1, Geoscientific Model Development, 3, 565–584, https://doi.org/10.5194/gmd-3-565-2010, 2010.

Weber, S. L., Drury, A. J., Toonen, W. H. J., and van Weele, M.: Wetland methane emissions during the Last Glacial Maximum estimated from PMIP2 simulations: Climate, vegetation, and geographic controls, Journal of Geophysical Research: Atmospheres, 115, D06 111, https://doi.org/10.1029/2009JD012110, 2010.

650 Zürcher, S., Spahni, R., Joos, F., Steinacher, M., and Fischer, H.: Impact of an abrupt cooling event on interglacial methane emissions in northern peatlands, Biogeosciences, 10, 1963–1981, https://doi.org/10.5194/bg-10-1963-2013, 2013.